

Crustal Structure Constraints from the Detection of the SsPp Phase on Mars

Jiaqi Li¹, Caroline Beghein¹, Paul Davis¹, Mark A Wiczorek², Scott M McLennan³, Doyeon Kim⁴, Ved Lekić⁵, Matthew Golombek⁶, Eleonore Stutzmann⁷, Philippe Lognonné⁷, William Bruce Banerdt⁶, and Martin Schimmel⁸

¹University of California, Los Angeles

²Université

³State University of New York at Stony Brook

⁴ETH Zürich

⁵University of Maryland

⁶California Institute of Technology

⁷Université de Paris

⁸Geosciences Barcelona (GEO3BCN - CSIC)

November 26, 2022

Abstract

The shallowest intracrustal layer (extending to 8 ± 2 km depth) beneath the Mars InSight Lander site exhibits low seismic wave velocity, which are likely related to a combination of high porosity and other lithological factors. The SsPp phase, an SV-to P-wave reflection on the receiver side, is naturally suited for constraining the seismic structure of this top crustal layer since its prominent signal makes it observable with a single station without the need for stacking. We have analyzed eight broadband and low-frequency seismic events recorded on Mars and made the first coherent detection of the SsPp phase on the red planet. The timing and amplitude of SsPp confirm the existence of the ~ 8 km interface in the crust and the large wave speed (or impedance) contrast across it. With our new constraints from the SsPp phase, we determined that the P-wave speed in the top crustal layer is between 2.5 km/s and 3.3 km/s, which is a more precise and robust estimate than the previous range of 2.0-3.5 km/s obtained by receiver function analysis. The porosity in Layer 1 is estimated to be as much as 21-31% (assuming an aspect ratio of 0.1 for the pore space), but could be lower if some pores are filled by low-density cements or other secondary 1 mineral phases. These porosities and P-wave speeds are compatible with our current understanding of the upper crustal stratigraphy beneath the InSight Lander site.

Supplementary Material of

Crustal Structure Constraints from the Detection of the SsPp Phase on Mars

Jiaqi Li, Caroline Beghein, Paul Davis, Mark. A. Wiczorek, Scott M. McLennan, Doyeon Kim, Ved Lekić, Matthew Golombek, Martin Schimmel, Eleonore Stutzmann, Philippe Lognonné, William Bruce Banerdt

Summary

There are 16 figures and 2 tables in this supplementary material.

We also discussed the following topics in this supplementary material:

1.1 Uncertainties

There are uncertainties (~ 5 degrees) in the epicentral distance of the recorded marsquakes (InSight Marsquake Service, 2020, 2021a, b, 2022a, b). Inaccurate epicentral distance will result in a deviated ray parameter and this error will propagate into the L2-norm misfit. To account for these uncertainties, we performed two grid searches, one with the minimum and one with the maximum epicentral distances. Results show that the derived L2-norm misfit map is very similar when using an uncertainty range of 5 degrees (Fig. S7). The final L2-norm misfit maps (Figs. 4 and 5) result from the summation of the cross-correlation maps of these two end-member epicentral distances.

There are also considerable uncertainties in the estimated back azimuth (Table S1), especially for the quality-B events. An incorrect back azimuth will influence the coordinate frame rotation from NEZ to RTZ, the particle motion analysis, and the subsequent separation of pseudo-P and pseudo-S components. In this study, we tried different back azimuth values within the ranges provided by Drilleau et al. (2021) and Zenhausern et al. (2022) and selected the one with the clearest SsPp signal. We also performed additional data processing, with the lower and upper limit of the back azimuth estimates from these previous studies. With the minimum back azimuth (Fig. S8a-c), the SsPp phases on the pseudo-P components for all eight events are almost unchanged (Fig. S8b). However, the pseudo-S components (Fig. S8a) are changed for three events (S0105a, S0484b, and S0918a), resulting in different pseudo-P waves after the deconvolution (Fig. S8c). When averaging the results from different events, we down-weighted these three events by half. When using the maximum back azimuth (Fig. S8d-f), three events (S0784a, S0407a, and S0802a) showed less observable SsPp phases and were therefore down-weighted by half.

Within this relatively large range of back azimuths, the pseudo-P waveforms for all eight events are almost identical. On the deconvolved pseudo-P components, either for the case with the minimum or maximum back azimuth, five of the eight show a stable SsPs phase compared with the waveforms utilized (Fig. 3), given variations in back azimuths of about 30 degrees. For the other three events, with extremely large variations in the back azimuths (e.g., larger than 70 degrees), the SsPp phase disappears, probably due to the wrong back azimuth, rather than shifts to another arrival time. This indicates that our identification of the SsPs phase at around 3.5 - 4.3 s is reliable over a wide range of back azimuths.

Much of the seismic data recorded by SEIS are affected by transient one-sided pulses called glitches, probably caused by internal thermal stresses from diurnal variations of the temperatures (Scholz et al., 2020). Glitches, if present in the time window of the S-wave reflections, can affect our analysis and the results. Although we removed these glitches from the selected seismic records following Scholz et al. (2020), to fully understand the possible influence of the glitches, we analyzed both the raw data and the deglitched data (Fig. S9). Among the eight events used in the SsPp studies, seven of them show no glitches within the time window. The only event influenced by a significant glitch (at around -2 seconds) is S0802a. Although this glitch does not interfere with the SsPp phase, it influences the particle motion analysis and adversely affects the source wavelet (pseudo-S) estimation. Consequently, in the raw data, although there is a negative pulse at around 4.5 seconds (Fig. S9a), this signal disappears after the deconvolution (Fig. S9c). In contrast, with the deglitched dataset used in this study, this negative pulse remains clear (Fig. S9c). Although the deglitched dataset behaves better for event S0802a, we cannot fully trust it since the removal of the glitches is dependent on the detection threshold, especially for smaller glitches (Scholz et al., 2020). Therefore, we further down-weighted the S0802a event by half.

1.2 Validation of the method

The separation of the pseudo-SV and pseudo-P wave trains is key to removing the source-side scatterings and enhancing the signals from the structure. In this study, we estimated those based on a particle motion analysis (Yu et al., 2012). This approach is fully based on the data, and does not rely on a priori knowledge of the near-surface. However, the results could be affected by the presence of noise.

Another way to separate the pseudo-S and pseudo-P wave trains is to estimate the upgoing P- and SV-waveforms using a free-surface transform matrix (Kennett, 1991) constructed from prior information about the P- and S-wave speeds of the near-surface and ray parameter of the wave. We chose the average P- and

S-wave speeds near the free surface from Kim et al. (2021) and performed a grid search to find ray parameter values that minimize the correlation between the P and SV waveforms computed within 2 s window centered around the S arrival. Results show that the derived pseudo-S and pseudo-P wave trains from this free-surface transformation are very consistent with those from the particle motion analysis (Fig. S10) for the same five events shown in Fig. 2. We also verified that the estimation from the free-surface transformation analysis is not strongly affected by ray parameter differences.

To further validate the accuracy of the derived source wavelet, we compared the SV-waves on the pseudo-S component (from the particle motion analysis) and the SH-waves on the tangential component for two events S0105a, and S0484b (Fig. S11). We should expect a similarity in the waveforms between the SV- and SH-waves since they both reflect the same source process. Results show that the cross-correlation coefficients between the SV- and SH-waves (time window from -3 s to 3 s) are 0.90 (for event S0105a, Fig. S11a1) and 0.73 (for events S0484b, Fig S11b1), despite a slight time shift (less than 1.5 s) that might be a result of seismic anisotropy in the crust (Li et al., 2022) and the mantle. We tested replacing the ‘pseudo-S’ wave trains with the SH-waves on the tangential component as the source wavelet and then performed the deconvolution. Results show that, with this different source wavelet, the SsPs phases are still clear and almost unchanged on both the radial and the ‘pseudo-P’ components for these two examples events (Fig. S11).

1.3 Validation of the results

In the current SsPp approach in the main text, we performed grid searches for three parameters (i.e., the average P-wave velocity in Layer 1, the thickness of Layer 1, and the P-wave velocity of the second layer) and obtained regions of acceptable models of Layer 1. Then, we compared these models with the models from the receiver function study to select the models that satisfy both types of data.

An alternative way to assess our results is to directly use the 40,000 receiver-function-derived models (Knapmeyer-Endrun et al. 2021) to calculate the synthetic SsPp waveforms and compare them with the SsPp data. To better illustrate this, we chose two typical events, S0484b, and S0918a, with maximum and minimum arrival times of about 3.75 and 4.20 s, respectively.

We found that although all the 40,000 models can satisfy the receiver function data, the fit to the SsPp data is quite variable (see Fig. S12a). Specifically, for both the 2-layer and 3-layer crustal models, the minimum L2-norm misfits (average value of events S0484b and S0918a) are around 0.7, and the maximum misfit can reach 3.0. The majority of the misfits are between 0.7 and 2.0.

Comparisons of synthetics and data show that, for the model with a low misfit of 0.8 (i.e., the red star in Fig. S12a), the synthetic waveform reproduces the negative phase at around 4 s. However, for a model with a misfit of 1.4 (i.e., the cyan star in Fig. S12a), the synthetics do not display the negative phase that is visible in the data (Fig. S12b-f). Based on a trial-and-error practice, we chose a misfit value of 1.1 as a threshold value for acceptable fitting solutions. Based on this threshold, the selected models are shown in Figs. S12d and S12g for the 2-layer and 3-layer crustal cases, respectively.

We note that, in this approach, all the model parameters are from the receiver-function-derived study (Knapmeyer-Endrun et al. 2021), and we did not perform a grid search for the velocity of the second layer. Nevertheless, the first-order pattern is consistent with the previous results in the main text: models with a P-wave velocity larger than 3.3 km/s are rejected. This implies that the upper limit of the P-wave velocity (at around 3.3 km/s) is required by the data and is not dependent on the inversion approaches.

1.4 Interferences with other signals

Phases that might interfere with the SsPs phase can come from both the source and the receiver sides. At the source side, depth phases (either free-surface reflection or under-side reflection off crustal layers) may have a similar arrival time as the SsPs phase. However, waveform complexity caused by depth phases would be present in both the direct SV wave and the SsPp phase. Since we deconvolved the pseudo-P trace using the assumed source wavelet (pseudo-S trace), this common feature is removed after the deconvolution (Yu et al., 2013).

On the receiver side, we only used a 1-layer crustal model in the waveform modeling because our SsPp data are most sensitive to the properties of Layer 1. However, the receiver function study found that there are at least two layers in the crust. To test whether or not the simplicity of our synthetic modeling is reasonable, we compared the waveforms on both the radial, vertical and pseudo-P components between models with one layer in the crust (the case we used in this study) and models with two layers (Fig. S13). Results show that the SsPs phase is not influenced by the signals from the deeper layer, since the major differences are before or after the SsPp phase. Interestingly, when the thickness of the second layer is 10 km, there is another negative phase arriving at 2 s. We have observed such a phase for many events (Fig. 3), but constraining the deeper layers is beyond the scope of this study.

1.5 Sharpness and dip of the interface

In both this study and the previous receiver function study (Knapmeyer-Endrun et al., 2021), the interface of Layer 1 was treated as a sharp discontinuity. This choice partly comes from the fact that we cannot effectively distinguish a sharp interface and a gradual one, given the size of the minimum resolvable wavelength, which is on the order of about 10 km.

To quantify how this assumption affects the inverted results in both the SsPp and the receiver function study, we performed synthetic tests where a gradual interface (with a width of 3 km) is given in the input model. In the first test (the P-wave speed of the second layer is 4.4 km/s), the inverted locations of the discontinuity for the SsPp and receiver function are both at the midpoint (at 8 km) of the gradual interface of the input model (Fig. S14c). Since the sharpness affects the SsPp and receiver function similarly, our previous derived P-wave speed ranges based on joint constraints from the SsPp and receiver function data are not influenced.

When the P-wave speed of the second layer is larger (e.g., 5.0 km/s in Fig. S14f), the inverted interface is still at the midpoint of 8 km for the receiver function case. However, for the SsPp case, the derived discontinuity is located at a slightly shallower depth (i.e., 7.6 km). This is because the SsPp phase is sensitive to the absolute velocity value, and the same P-wave speed can be achieved at a somewhat shallower depth (i.e., 7.6 km) when the velocity of the second layer is larger. In this case, the thickness of Layer 1 will be underestimated in the SsPp case, compared with the receiver function study (Knapmeyer-Endrun et al., 2021). Therefore, if the interface is gradual, the acceptable regions (e.g., the shaded regions in Fig. 6) from the SsPp analysis should move to a slightly larger thickness. Moving the acceptable regions to a larger thickness will result in a smaller threshold for the P-wave speed, therefore, our previous conclusion that models with a P-wave velocity larger than 3.3 km/s are rejected is still valid.

Given the large uncertainties in the back azimuths of the marsquakes, it is challenging to resolve the dip of the interface. In addition, the effect of the tilt is not as pronounced for Layer 1 on Mars as it is for the Moho on Earth. This is because the location of the point where the SsPp wave enters Layer 1 on Mars (the base of which is located at about 8 km) is only about 15 km horizontally from the station, which is smaller than the case for the Moho on Earth (located at a deeper depth).

1.6 Effects of different data types

The current analyses are based on displacement records because there are fewer oscillations compared with velocity records. However, on Earth, velocity records are also used for receiver function studies. To test the effects of different data types on the results, we have reproduced the analysis using the velocity data for all eight events.

Fig. S15a shows that there are higher frequency signals in the radial and vertical components for the velocity results (in red), compared with the displacement results (in black). But after the deconvolution (Fig. S15b), the pseudo-P waveforms for both the velocity and displacement results are almost the same for seven events except for S0784a. Therefore, different data types do not change our results.

1.7 Comparison with auto-correlations

The auto-correlation of the continuous records (noise or seismic coda wave) can be used to derive empirical

Green’s functions, which provide independent constraints on the underlying structure. We gathered auto-correlation results from Compaire et al. (2021) and Schimmel et al. (2021) and focused on arrivals close to the SsPp phase of Layer 1. For each arrival, we assumed its uncertainty to be half of the longest period used in that study and then used ray theory to derive the acceptable regions of the model space from equation (1).

These supplementary constraints from the vertical auto-correlation studies are shown (as shaded regions) in Fig S10. For the vertical auto-correlation, arrivals corresponding to Layer 1 are 5.6 ± 0.5 seconds (Compaire et al., 2021) and 6.15 ± 0.42 seconds (Schimmel et al., 2021). The derived acceptable regions from these vertical auto-correlations are of a similar trend when compared with the models from the receiver function study and therefore do not provide new constraints on the P-wave speed models (Fig. S16a and b). This might be due to the relatively large uncertainty we assumed, or because of the vertical ray path of the auto-correlation. The auto-correlation-derived acceptable regions intersect with our reflection-derived regions, further confirming our results. The different trends of these two regions reflect different ray parameters between the auto-correlation and reflections from teleseismic events.

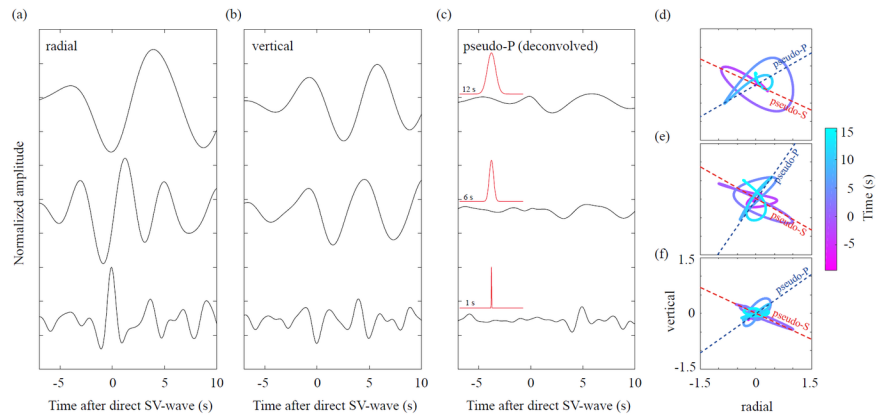


Figure S1. Synthetic tests of the influence of the length of the source wavelet.

- (a) Waveforms on the radial component with different lengths of the source time function, using orthonormal propagator algorithm, QSEIS (Wang, 1999).
- (b) Same as (a), on the vertical component.
- (c) Waveform (in black) on the pseudo-P component (after deconvolution). The red traces show the source time function used with different durations (i.e., 1 s, 6 s, and 12 s).
- (d) Particle motion analysis for traces in (a) and (b). The layout is the same as Fig. 1c.

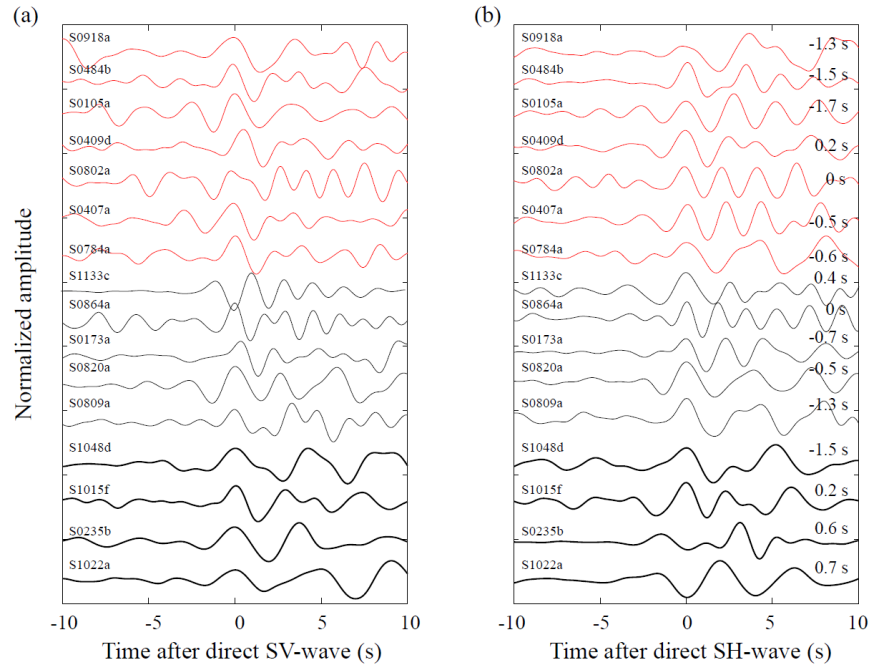


Figure S2. Source wavelets for quality-A events (four with longer source wavelet are in thick black lines, the other five are in thin black lines), and quality-B events (in red) for the SV-waves (a) and SH-waves (b), respectively.

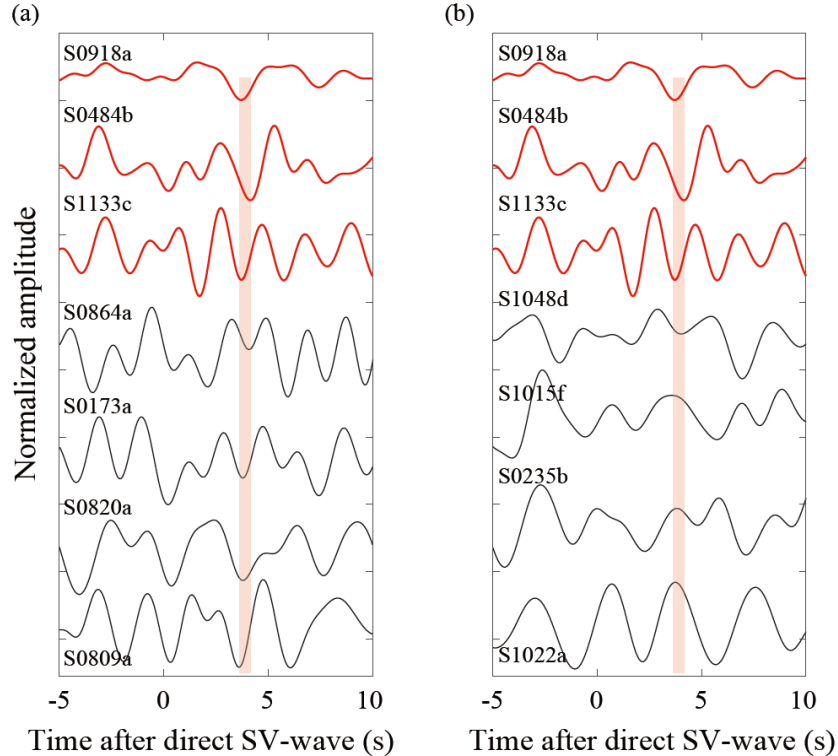


Figure S3. Comparison of the pseudo-P trace (after deconvolution) between the events used in this study (in red) and other quality-A events (in black) with shorter source duration (a) and longer source duration (b). The vertical shaded bar marks the location of the negative picks of these three events used in this study (in red).

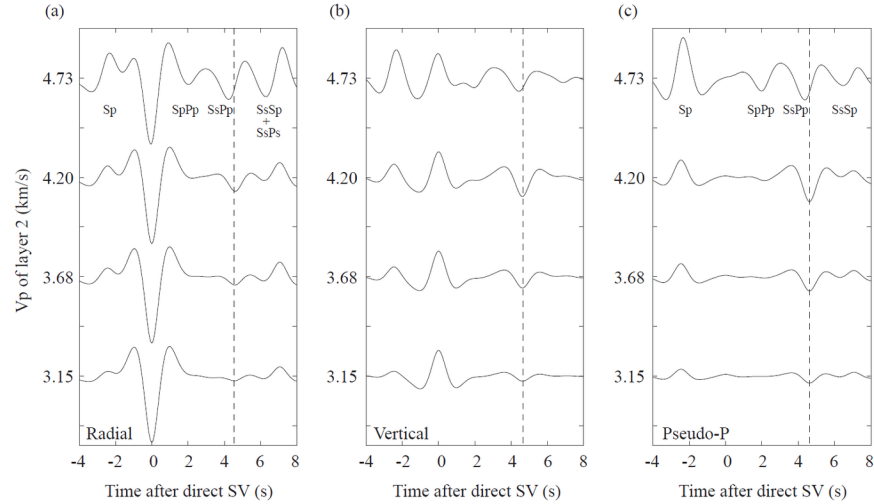


Figure S4. Synthetic tests of the influence of the velocity in the second layer.

- (a) Displacement waveforms on the radial component with different velocities of the second layer. The dashed vertical line marks the arrival time of the SsPp phase, calculated using ray theory from formula (1).
- (b) Same as (a), on the vertical component.
- (c) Same as (a), on the pseudo-P component.

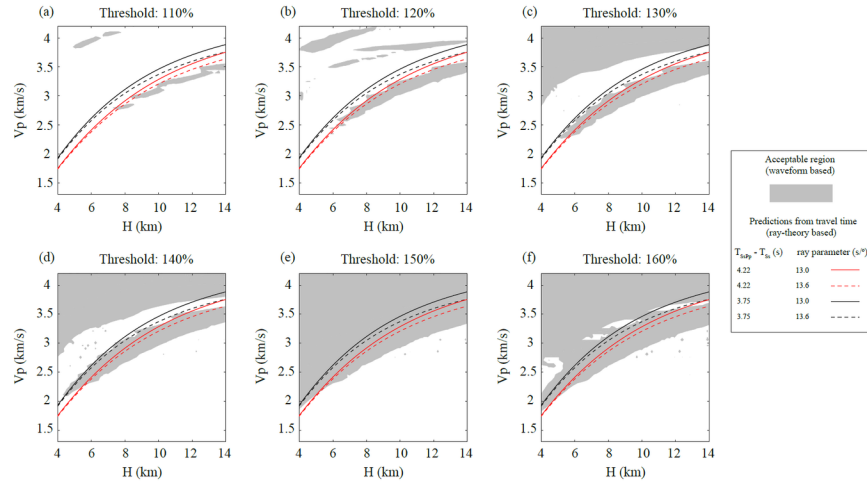


Figure S5. Model constraints from the SsPp phase with different thresholds of the L2-norm misfit.

(a) Acceptable model region (in grey), derived from Fig. 5a, with a threshold of 110% of the minimum misfit. The red and black curves are predictions from ray theory with different ray parameters and differential travel time between the direct Ss and SsPp phase.

Similar analysis for threshold of (b) 120%, (c) 130%, (d) 140%, (e) 150%, and (f) 160%.

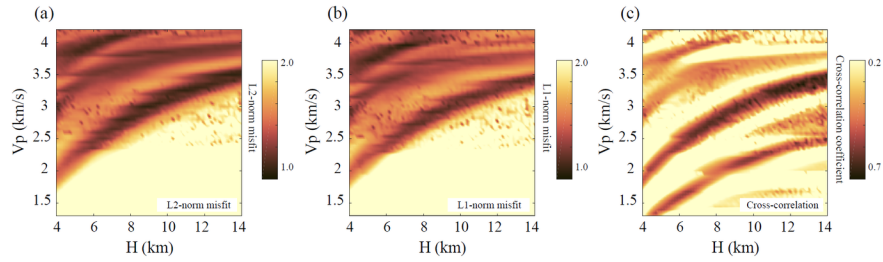


Figure S6. Synthetic tests of the influence of the choice of the misfit measurements

- (a) Misfit map for L2-norm.
- (b) Misfit map for L1-norm.
- (c) Misfit map for cross-correlation coefficient.

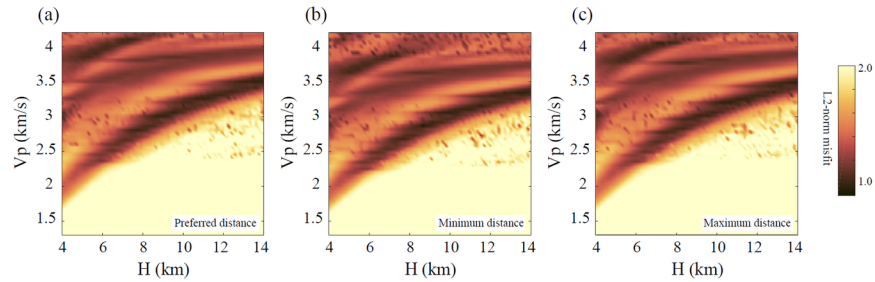


Figure S7. Synthetic tests for the influence of the epicentral distance. The summed L2-norm misfit map with the preferred epicentral distance (a), the minimum epicentral distance, and the maximum epicentral distance (values are listed in Table S1).

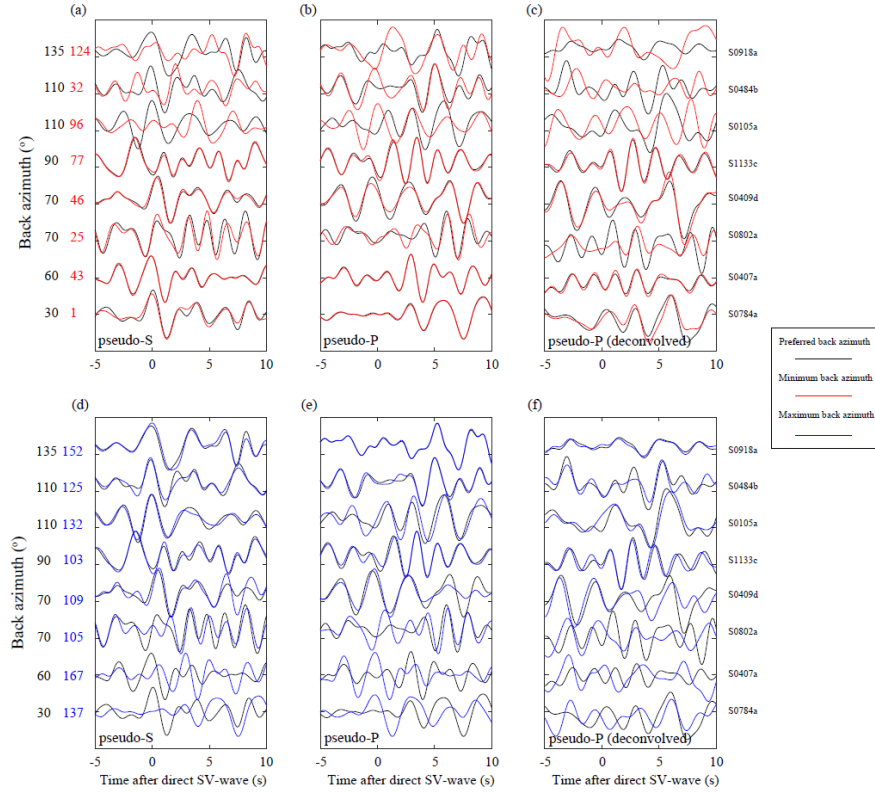


Figure S8. Waveforms on the pseudo-S, pseudo-P, and pseudo-P (after deconvolution) components with the preferred back azimuths (in black), the minimum back azimuths (in red), and the maximum back azimuths (in blue). The range of the back azimuth is listed in Table S1.

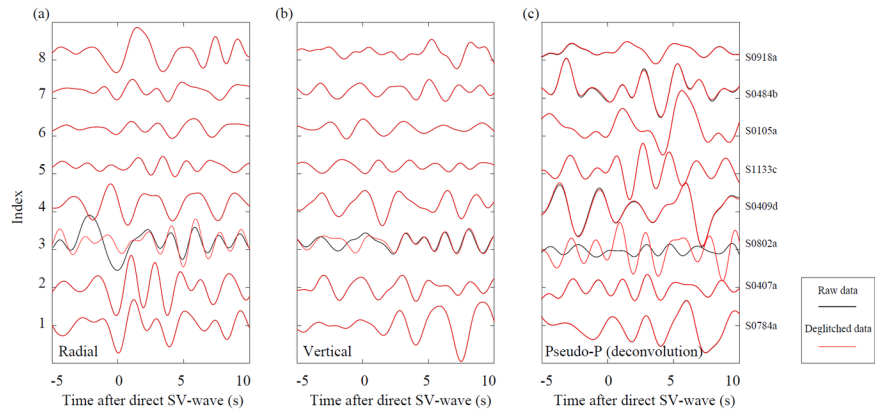


Figure S9. Tests for the influence of glitches. Waveform comparisons on the radial (a), vertical (b), and the pseudo-P (after the deconvolution) (c) components for the raw data (in black) and deglitched data (in red).

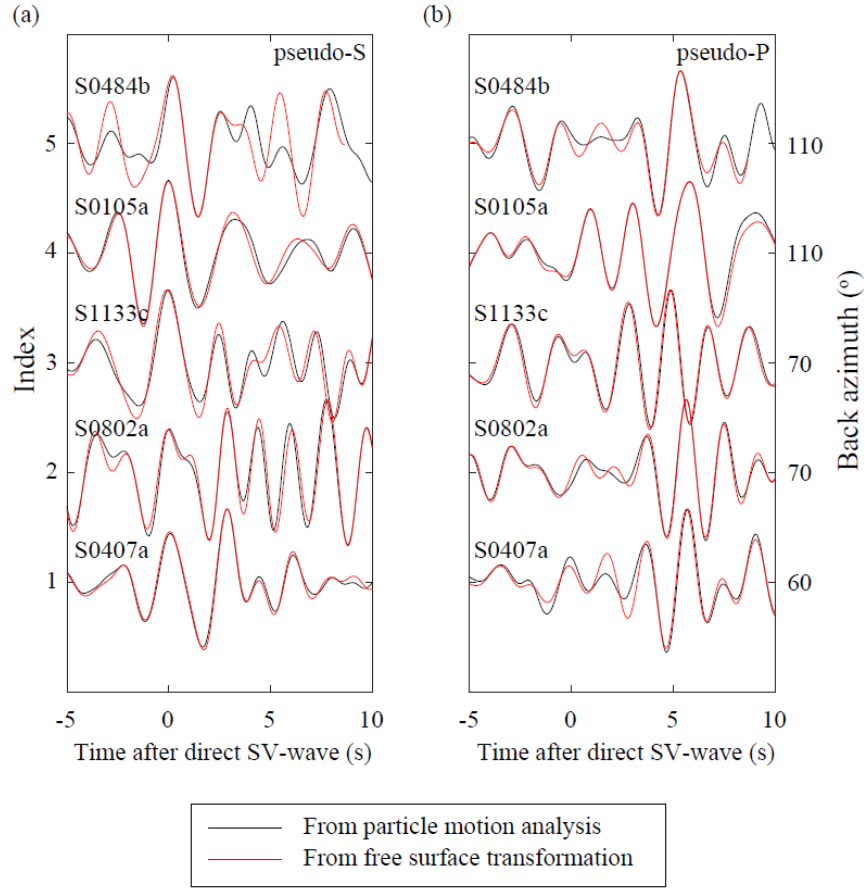


Figure S10

(a) Comparison of the pseudo-S wave trains from the particle motion analysis (in black) and from the free-surface transformation (in red) for the same events (i.e., S0105a, S0407a, S0484b, S0802a, and S1133c) shown in Fig. 2.

(b) Similar to (a), but for the pseudo-P wave trains.

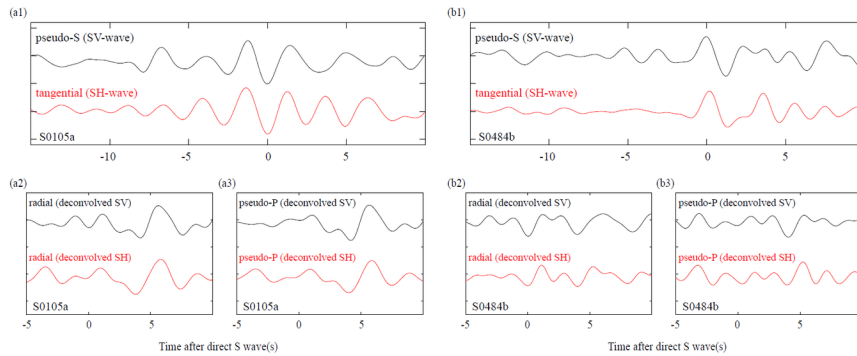


Figure S11

(a1) Comparison of the source wavelets on the pseudo-S component (in black) and the tangential component (in red). A time shift of 1 s is applied to the tangential component for this event S0105a.

(a2) Comparison of the SsPp phases on the radial components after the deconvolution, with the SV-waves as the source wavelet (in black), and the SH-waves as the source wavelet (in red).

(a3) Similar to (a2), but for the ‘pseudo-P’ components after the deconvolution.

(b1-b3) Similar to (a1-a3), but for the event S0484b, with a time shift of -1.5 s.

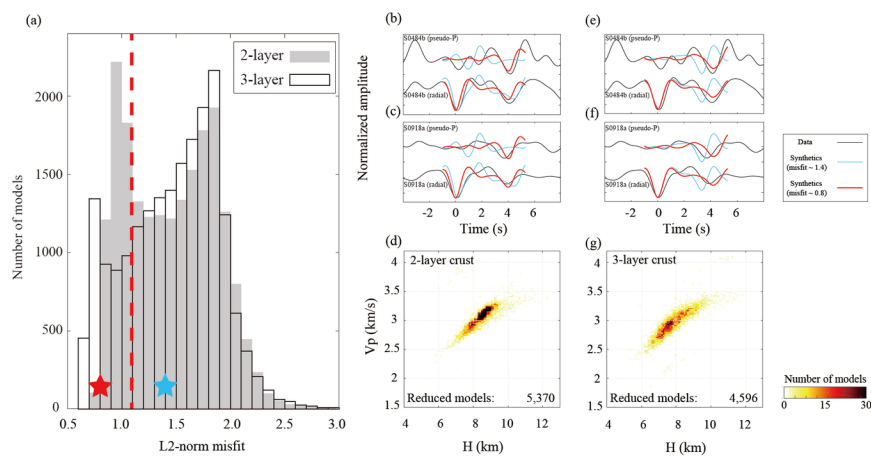


Figure S12

1. Histogram of the L2-norm misfit for the 20,000 models in both the 2-layer (in shaded grey) and 3-layer crustal cases (in black). The dashed red line indicates the L2-norm misfit of 1.1, which is the threshold used in (d) and (g). The blue (with L2-norm misfit of 1.4) and red (with L2-norm misfit of 0.8) stars mark the index of the model selected to generate the synthetics shown in the right panels.
2. Waveform comparison between the data (in black), and the synthetics (for the 2-layer crustal case) with misfit values of 0.8 (in red) and 1.4 (in blue) on the pseudo-P and radial components (after deconvolution) for event S0484b.
3. Same as (b), for event S0918a.
4. Selected models with L2-norm misfits smaller than 1.1 for the 2-layer crustal case.

(e-g) Same as (b-d), for the 3-layer crustal case.

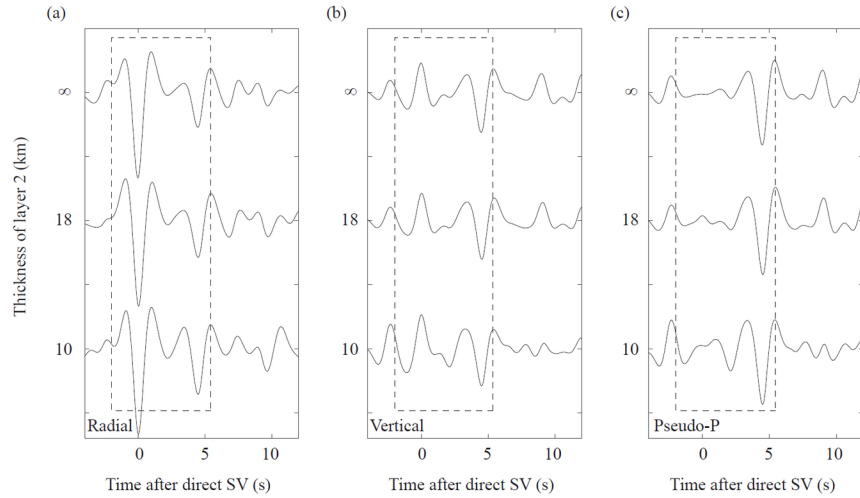


Figure S13. Synthetic tests of the influence of the thickness of the second layer.

(a) Displacement waveforms on the radial component with different thicknesses of the second layer. The dashed box marks the time window used in this study.

(b) Same as (a), on the vertical component.

(c) Same as (a), on the pseudo-P component.

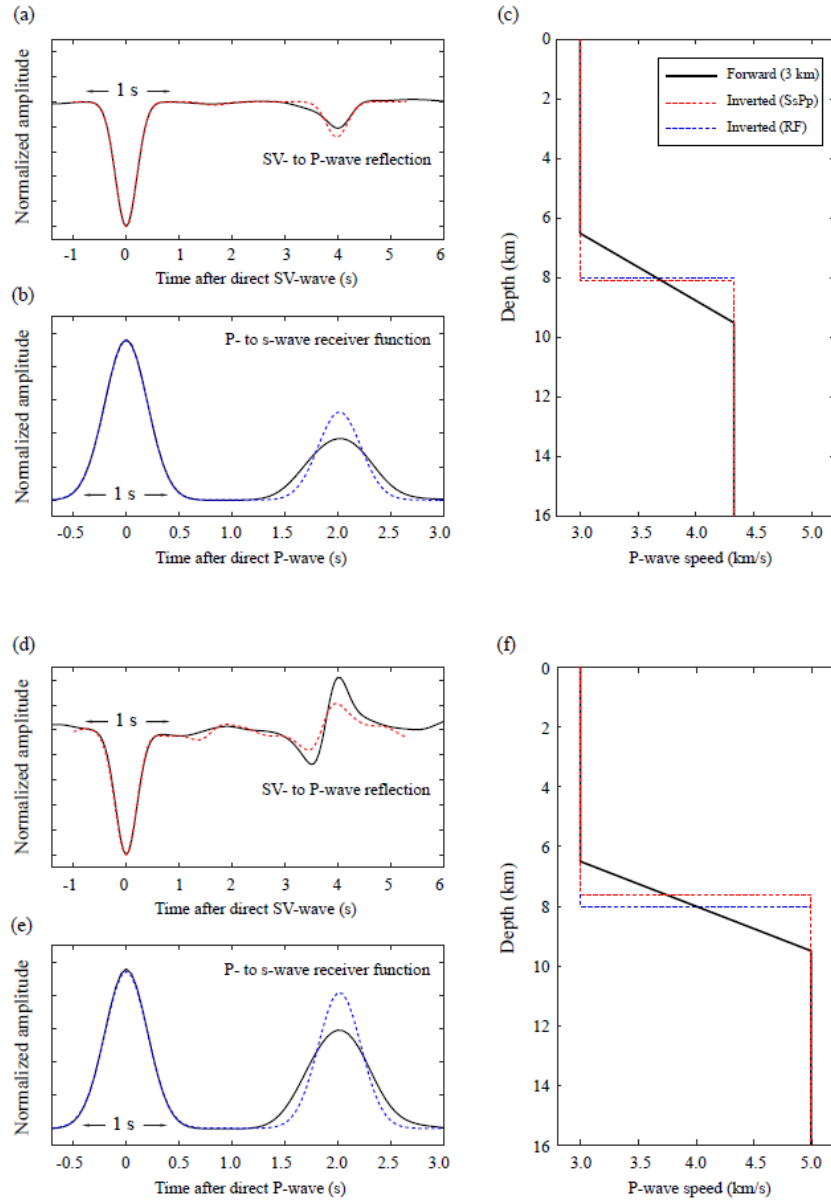


Figure S14. Synthetic tests for the sharpness of Layer 1.

1. Synthetic waveforms (i.e., SsPp at around 4 s) on the radial component after the deconvolution. The solid black, and dashed red waveforms correspond to the ground truth model (gradual interface), and the inverted model (sharp interface), respectively, with the same color in (c).
2. Synthetic P- to s-wave receiver functions, the layout is similar to (a). Note that the time axis is stretched for better comparison with (a).
3. Input and output (inverted) models. The solid black model has a gradual interface (centered at 8.0 km with a thickness of 3 km), and the P-wave speed of the second layer is fixed at 4.3 km/s. The synthetic waveform calculated with this gradual model is viewed as synthetic data for this test. The dashed red and blue lines represent the inverted models (assuming a sharp interface during the grid search), for the SsPp and the P- to s-wave receiver function cases, respectively. These inverted models

are the ones corresponding to the minimum L2-norm misfit among all the candidate models resulting from the grid search.

(d-e) similar to (a-c), but with a larger P-wave speed (i.e., 5.0 km/s) of the second layer.

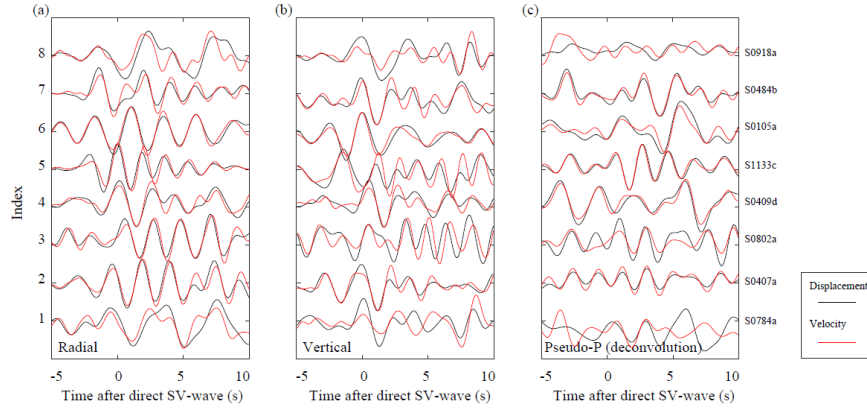


Figure S15. Effects of different data types

- (a) The displacement records (in black) and the velocity records (in red) on the radial component.
- (b) Similar to (a) but on the vertical component.
- (c) Similar to (a) but on the pseudo-P component, after the deconvolution.

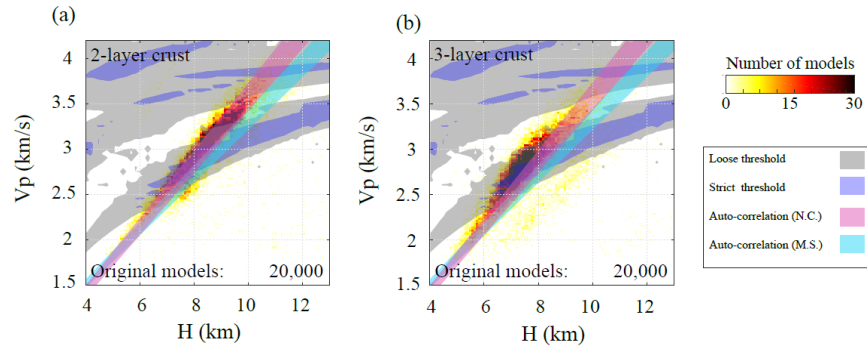


Figure S16. Acceptable model regions from two auto-correlation studies of Compaire et al. (2021) and Schimmel et al. (2021) were illustrated by the pink and cyan regions, respectively. Other layouts are the same as Fig. 6a.

Table S1 Events selected for SV- to P-wave reflections

Event Name	Event Type	Distance(°)	$T_c - T_p$ (s)	Back Azimuth 1°(°)	Back Azimuth 2°(°)	Back Azimuth 3°(°)	Back Azimuth 4°(°)	$T_{s2p} - T_p$ (s)
S0105a	B. Low Frequency	31.4 [- 5.3, + 5.3]	188	N/A	112.1 [-16.0, +20.2]	N/A	110	4.25
S0407a	B. Low Frequency	28.5 [- 1.8, + 1.8]	171	N/A	57.0 [-14.0, +112.0]	79.0 [-24.5, +26.0]	60	4.00
S0409d	B. Low Frequency	30.2 [- 4.7, + 4.7]	181	N/A	70.0 [-20.0, +20.0]	82.7 [-28.7, +26.1]	70	3.50
S0484b	B. Broad Band	30.8 [- 4.7, + 4.1]	184	N/A	100.0 [-20.0, +20.0]	73.4 [-41.3, +37.9]	110	4.20
S0784a	B. Broad Band	33.2 [- 3.0, + 3.0]	200	N/A	115.5 [114.7, +21.1]	101.2 [-23.6, +22.8]	30	4.05
S0802a	B. Broad Band	29.1 [- 2.4, + 3.0]	175	N/A	81.8 [-56.5, +14.0]	85.2 [-19.5, +20.0]	70	3.95
S0918a	B. Low Frequency	26.1 [- 3.0, + 3.0]	158	N/A	137.4 [-13.5, +14.3]	N/A	135	3.80
S1133c	A. Broad Band	30.0 [- 1.1, + 1.1]	176	90.0 [-13.0, +13.0]	N/A	N/A	90	3.70

* From InSight Marsquake Service (2020, 2021a, b, 2022a, b)

** From Zenhansen et al. (2022)

*** From Drilleau et al. (2021)

**** From this study, according to the clearest separation of the pseudo-P and pseudo-S components, and the identification of the S_{2p} phase on the pseudo-P component.

Table S1. Events selected for the SsPp phase in this study: one quality-A event and seven quality-B events. The values for epicentral distance, back azimuth, and differential travel time between P- and S-waves are also included. The measured travel time differences between the direct Ss wave and the SsPp (from this study) and the preferred back azimuth (from this study) are listed in the last two columns.

Table S2 Events information and the corresponding parameters used in this study

Event Name	Event Type	Absolute origin (MQS)	SAC origin (s)	S arrival 1' (s)	S arrival 2' (s)	PM_b (s)	PM_e (s)	STF_b (s)	STF_e (s)	Distance* (°)	Back azimuth* (°)
S0105a	B, Low Frequency	2019-03-14T20:59:21	1578.0	438	431.7	-5.0	10.0	-10.0	10.0	30	110
S0407a	B, Low Frequency	2020-01-19T09:54:02	3691.2	394	393.0	-5.0	8.0	-3.0	8.0	30	60
S0409d	B, Low Frequency	2020-01-21T11:27:02	3603.3	424	425.9	-10.0	10.0	-10.0	10.0	27	70
S0484b	B, Broad Band	2020-04-07T08:48:20	3600.9	428	428.5	-5.0	10.0	-6.0	6.0	31	110
S0784a	B, Broad Band	2021-02-09T12:11:32	3600.7	464	462.5	-5.0	11.0	-7.0	12.0	33	30
S0802a	B, Broad Band	2021-02-28T06:07:21	1800.0	404	398.0	-5.0	11.0	-4.0	5.0	29	70
S0918a	B, Low Frequency	2021-06-27T05:31:55	3603.0	367	367.0	-5.0	7.3	-5.6	16.0	26	135
S1133c	A, Broad Band	2022-02-03T08:04:36	3603.3	404	406.8	-10.0	10.0	-10.0	6.0	30	90

* From InSight Marsquake Service (2020, 2021a, b, 2022a, b)
 ** From this study

Table S2. Key parameters for the eight events analyzed in this study. Besides the information shown in Table S1, other important parameters include: ‘absolute origin’, which marks the start time of the marsquake and is provided by MQS in the UTC format. ‘SAC origin’ indicates the start time of the SAC file (provided in the supplementary material) before the origin time. The arrival time of the direct S-wave from MQS and this study are both listed in the fifth and sixth columns, respectively. ‘PM_b’ and ‘PM_e’ mark the begin and end-time of the time window used in the particle motion analysis. ‘STF_b’ and ‘STF_e’ denote the begin and end time of the time window used during the deconvolution.

Hosted file

essoar.10512137.1.docx available at <https://authorea.com/users/526041/articles/605542-crustal-structure-constraints-from-the-detection-of-the-sspp-phase-on-mars>

Crustal Structure Constraints from the Detection of the SsPp Phase on Mars

Jiaqi Li^{1*}, Caroline Beghein¹, Paul Davis¹, Mark. A. Wieczorek², Scott M. McLennan³, Doyeon Kim^{4, 5}, Ved Lekić⁵, Matthew Golombek⁶, Martin Schimmel⁷, Eleonore Stutzmann⁸, Philippe Lognonné⁸, William Bruce Banerdt⁶

¹ Department of Earth, Planetary, and Space Sciences, University of California, Los Angeles, CA 90095, USA. E-mail: jli@epss.ucla.edu

² Université Côte d’Azur, Observatoire de la Côte d’Azur, CNRS, Laboratoire Lagrange, Nice, France

³ Department of Geosciences, Stony Brook University, Stony Brook, New York, 11794-2100 USA

⁴ Department of Earth Sciences, Institute of Geophysics, ETH Zürich, Zürich, Switzerland

⁵ Department of Geology, University of Maryland, College Park, Maryland, USA.

⁶ Jet Propulsion Laboratory, California Institute of Technology, Pasadena, CA 91109, USA.

⁷ Geosciences Barcelona - CSIC, Barcelona, Spain.

⁸ Université de Paris, Institut de physique du globe de Paris, CNRS, Paris, F-75005, France.

Abstract

The shallowest intracrustal layer (extending to 8 ± 2 km depth) beneath the Mars InSight Lander site exhibits low seismic wave velocity, which are likely related to a combination of high porosity and other lithological factors. The SsPp phase, an SV- to P-wave reflection on the receiver side, is naturally suited for constraining the seismic structure of this top crustal layer since its prominent signal makes it observable with a single station without the need for stacking. We have analyzed eight broadband and low-frequency seismic events recorded on Mars and made the first coherent detection of the SsPp phase on the red planet. The timing and amplitude of SsPp confirm the existence of the ~ 8 km interface in the crust and the large wave speed (or impedance) contrast across it. With our new constraints from the SsPp phase, we determined that the P-wave speed in the top crustal layer is between 2.5 km/s and 3.3 km/s, which is a more precise and robust estimate than the previous range of 2.0 - 3.5 km/s obtained by receiver function analysis. The porosity in Layer 1 is estimated to be as much as 21-31% (assuming an aspect ratio of 0.1 for the pore space), but could be lower if some pores are filled by low-density cements or other secondary

mineral phases. These porosities and P-wave speeds are compatible with our current understanding of the upper crustal stratigraphy beneath the InSight Lander site.

Keywords Martian crust, porosity, marsquake, P-wave speed

Key Points:

- We analyzed marsquakes and made the first coherent detection of the SsPp phase (an SV- to P-wave reflection on the receiver side).
- We determined that the P-wave speed in the top crustal layer (Layer 1, above 8 km) is between 2.5 km/s and 3.3 km/s
- The P-wave speed in Layer 1 is consistent with the current understanding of the upper crustal stratigraphy beneath InSight.

Plain Language Summary

The NASA InSight mission sent a seismometer to Mars in 2018. One of the science goals of the mission is to better understand how rocky planets form and evolve by investigating the interior structure of Mars. Previous seismological studies with InSight data have revealed a shallow crustal layer (i.e., Layer 1, extending to 8 ± 2 km depth) with low seismic wave speed under the instrument. In this study, we have identified a new seismic signal on the seismograms recorded on Mars. The existence of this seismic phase confirmed the low speed of compressional (P) waves in Layer 1 and provided additional constraints on the P-wave speed, i.e., between 2.5 km/s and 3.3 km/s. Based on these low speeds, we found that the seismic properties of Layer 1 likely result primarily from the presence of sedimentary rocks and/or aqueously altered igneous rocks that also have a significant amount of porosity, possibly as much as ~30% by volume. These porosities and P-wave speeds are compatible with our current understanding of the upper crustal stratigraphy beneath the InSight Lander site.

Introduction

One of the science goals of the NASA InSight mission is to better understand how rocky planets form and evolve by investigating the interior structure of Mars (Banerdt et al. 2020). Since the landing in November 2018, the Seismic Experiment for Interior Structure (SEIS, Lognonné, et al., 2019) Very Broadband (VBB) seismometer has recorded more than one thousand events (InSight Marsquake Service, 2020, 2021a, b, 2022a, b). Preliminary models of the crust and mantle structure, as well as core size, have been obtained with receiver function analysis (Lognonné et al., 2020; Kim et al., 2021; Knapmeyer-Endrun et al., 2021), P- and S-wave differential travel-times and surface-reflected body-wave phases (Khan et al., 2021), and ScS waves (Stähler et al., 2021), respectively.

Using P-to-s receiver functions, Knapmeyer-Endrun et al. (2021) found two possible sets of crustal models at the lander site: a 2-layer model with a crustal thickness of 20 ± 5 km and a 3-layer model with a thickness of 39 ± 8 km depth (with a weaker impedance contrast across it). Kim et al. (2021a) subsequently found that both S-to-p receiver functions and receiver functions constructed from free-surface P-wave multiples (PPs) favor the 3-layer model. Durán et al. (2022) also supported the 3-layer model using a more complete marsquake catalog and phase picks, though with slightly different average interface depths of 10 km, 20 km, and 45 km. Using ambient noise auto-correlation, Deng & Levander (2020), Schimmel et al. (2021), and Kim et al. (2021b) observed the strongest signal at a lag time of 10.6 s, which corresponds to a discontinuity at about 21 km depth, in agreement with the observed receiver function amplitudes.

Another prominent teleseismic signal well-recorded on Earth and often used to constrain the depth of the Mohorovičić discontinuity (hereafter referred to as Moho) is the SsPp phase, an SV- to P-wave reflection off the free surface on the receiver side. For incoming S-waves (i.e., SV-wave) polarized in the P-SV plane containing the event and the receiver, phase conversion occurs at the free surface and the converted P-waves reflect at the Moho (or any other intracrustal discontinuity) before being recorded by the seismometer (Fig. 1b). On Earth, this SsPp phase has been analyzed in data from isolated stations (e.g., Zandt and Randall, 1985; Owens and Zandt 1997; Zhou et al., 2000) and seismic arrays (Tseng et al., 2009; Yu et al., 2012; Chen and Jiang, 2020) to constrain crustal thickness. Cunningham and Lekic (2019) and Liu et al. (2019) additionally showed that SsPp phases provide complementary constraints that remove the trade-off between velocity and thickness inherent in receiver function analysis. Because there is a near-critical (sometimes post-critical) reflection within the top layer, the SsPp phase is usually stronger than an SV- to p-wave conversion in the conventional S-wave receiver function (Chen and Chen, 2019), and has been observed in several regions on Earth. For example, SsPp phases arrive at 4–11 s after the direct SV-phase in the western United States (Yu et al., 2016), 7–12 s across the North China craton (Yu et al., 2012), and 12–18 s across the Himalayan-Tibetan orogeny (Tseng et al., 2009).

In continental regions on Earth, the Moho lies between depths of about 15 km and 75 km (e.g., Brown and Mussett, 1993; Chen et al., 2013; Laske et al., 2013). When there are no sedimentary basins, the Moho is usually where the most significant jump in seismic wave speed occurs within the lithosphere of the average Earth model (e.g., Kennett and Engdahl, 1991). At the Mars InSight lander site, the situation is different, and the interface with the largest wave speed change corresponds to the shallowest intracrustal layer, hereafter referred to as Layer 1, at 8 ± 2 km (Knapmeyer-Endrun et al., 2021). The velocity contrast is estimated to be up to +40% due to the relatively low wave velocity within Layer 1.

The low velocity and recently discovered radial anisotropy of Layer 1 (Li et al., 2022), make it an important region to study since both features are likely related

to high porosity in the Martian crust (Knapmeyer-Endrun et al., 2021; Li et al., 2022). The low observed velocities could potentially be a result of sedimentary or volcanic ash and pyroclastic deposits that have intrinsically high porosity, or a high density of fractures in the upper crust generated by impact cratering events, such as is observed on the Moon (e.g., Wieczorek et al. 2013, Milbury et al. 2015, Soderblum et al. 2015). Alternatively, the low velocities could be the result of a high quantity of aqueously altered materials (Lognonné et al., LPSC, 2022). Understanding the origin of the low seismic velocity in this layer would not only provide clues to the origin of this layer but would also provide useful information for future studies of the deeper crustal layers (e.g., Wieczorek et al. 2022).

The large amplitude characteristics of SsPp and the previously-observed large wave speed jump across the base of Layer 1 make the SsPp an ideal phase to further constrain the properties of Layer 1. In addition, because it can be observed with a single station without the need for stacking, this phase is naturally suitable for seismic studies on Mars where we only have one instrument at a single location on the planet.

Data and Methods

There are two main criteria for SsPp data selection on Earth. First, the epicentral distance should be larger than 30 degrees to avoid mantle triplications generated by the 410-km and 660-km discontinuities (Kang et al., 2016). On Mars, the ideal epicentral distance to detect SsPp should be smaller than 60 degrees, since the olivine-to-wadsleyite phase transformation occurs at around 800-1100 km depths (Stähler et al., 2021; Huang et al., 2022).

Second, the source wavelet should be simple. Deep earthquakes are therefore usually preferred (e.g., Tseng et al., 2009) since their source time function is often simple, and the depth phases from deep earthquakes, which arrive later, do not interfere with SsPp. This criterion could have been a problem to detect SsPp on Mars since most of the events detected so far likely originate from depths shallower than 40 km (Drilleau et al., 2021; Durán et al. (2022)). Nevertheless, Yu et al. (2013) showed that this problem could be mitigated by removing the source wavelet complexity resulting from source-side scattering. Specifically, analyses of particle motion provide clues for deriving a ‘pseudo-S’ wave train, which contains information about both the source time function and depth phases. After the deconvolution of this ‘pseudo-S’ wave train, the authors showed that shallow events with complex source wavelets display signals in the seismic data of similar clarity to those from deep earthquakes (Yu et al., 2013). This method thus greatly increases the number of earthquakes that can be used to study SsPp phases and makes it possible to look for them on Mars.

In addition to these two criteria, we found that the duration of the source wavelet, which is measured based on the direct SV phase (Ss), plays a crucial

role in reliably detecting SsPp phases on Mars, and that it needs to be relatively short. On Earth, the SsPp phase is mostly used to study the Moho and arrives at relatively large differential travel times between the Ss and SsPp phases (e.g., 4 – 11 s in the western United States (Yu et al., 2016)). This implies that even a relatively long source wavelet duration does not affect the SsPp detection. On Mars, however, the base of Layer 1 is located at about 8 km depth and synthetic waveforms (where the source time function has a short duration of 1 s) predict differential arrival times of only about 4 s (Fig. 1c). This means that if the source time function has a relatively long duration, the SsPp phase will likely be buried in the Ss phase source wavelet, making it undetectable directly (Fig. S1). We verified that as long as the duration of the source wavelet is less than $T_{\text{SsPp}} - T_{\text{Ss}}$, the particle motions show linear trends and the source-normalization technique (Yu et al., 2013) can effectively obtain the corresponding SV-to-P-phase (e.g., Fig. S1f). On the contrary, if the duration of the source wavelet is larger than $T_{\text{SsPp}} - T_{\text{Ss}}$, the particle motions no longer exhibit linear trends (Fig. S1d and 1e), and the short time function approximation cannot be applied, in which case the derived SsPp phase is unreliable (Fig. S1c).

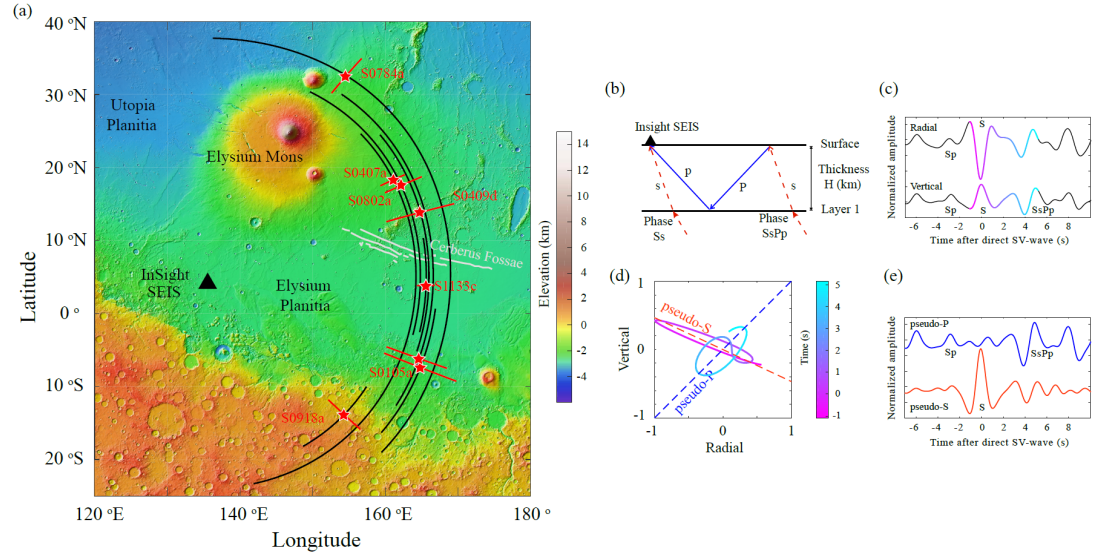
Locating marsquakes using a single station is challenging because both the arrival times of P- and S-waves and P-wave polarization information are needed to determine the epicentral distance and the back azimuth, respectively. During 1,133 Mars solar days (i.e., over three Earth years), SEIS has recorded 32 broadband (with energy up to 2.4 Hz) and 52 low-frequency (with energy below 1 Hz) marsquakes, and only 11 of them are labeled “quality-A” by the InSight Marsquake Service (MQS) (2020, 2021a, b, 2022a, b). To be designated quality-A, an event needs to have both clear back azimuth and epicentral distance. Quality-A marsquakes, in most cases, are ideal candidates for many seismological studies due to the strong seismic energy, high signal-to-noise ratio, and well-constrained event location. However, most of the quality-A events happen to have relatively long and complex source wavelets, therefore, are not necessarily ideal for analyzing SsPp phases.

To date, nine quality-A events have an epicentral distance smaller than 60 degrees. Four of them (S0235b, S1015f, S1022a, and S1048d) exhibit very long (e.g., larger than 5 s) and complex source wavelets, indicating that they are not suitable for our SsPp study (Fig. S2). There is less low-frequency content in the source time function of the other five quality-A events (S0173a, S0809a, S0820a, S0864a, and S1133c) and although multiple peaks or oscillations are observed, they are potential candidates for this study (Fig. S2).

Compared with quality-A events, marsquakes of quality B, in general, have shorter and simpler source wavelets. There are 18 marsquakes of quality B (eight broadband and 10 low-frequency), and the epicentral distance has been measured to be within 60 degrees (with an uncertainty smaller than 10 degrees) for 12 of them. However, due to their relatively low signal-to-noise ratio, the MQS has not determined the back azimuth for the quality-B events. Recent studies by Drilleau et al. (2021) and Zenhausern et al. (2022) with detailed

analyses of the waveforms provided back azimuth estimates for 10 of these 12 events. After excluding event S0325a whose estimated back azimuth shows large discrepancies between the two studies, we are left with a total of nine quality-B events with both epicentral distance and back azimuth information.

In this study, we focused on seven of these nine quality-B events with back azimuths between 0 to 180 degrees (Table S1) and which are in the same direction (to the east of the InSight lander) as the events used in the receiver function study (Knapmeyer-Endrun et al., 2021). Besides these seven quality-B events (Fig. 1a), we also included quality-A event S1133c, which has a relatively short source time function of ~ 4 s. Comparisons with the other eight quality-A events can be found in the Supplementary Material (i.e., Fig. S2 and S3).



1.1 Data Processing

The waveform data (InSight SEIS data service, 2019) were processed by first applying a pre-filtering from 0.01 to 8 Hz (zero-phase, 2nd order Butterworth filter) to the deglitched dataset (Scholz et al., 2020, with a sampling rate of 20 samples per second), and then removing the instrument response to get the ground motion records. Finally, we filtered (zero-phase, 2nd order Butterworth filter) the data into periods from 1.5 s to 6 s. We prefer working with the displacement record because there are fewer oscillations compared with the velocity record.

To analyze the SsPp, we need to use data from the radial (R) and vertical (Z) components. We thus converted the waveforms from the original UVW to NEZ channels using ObsPy (Beyreuther et al., 2010) and rotated the coordinates from NEZ to RTZ using the back azimuth information provided by previous

studies (Drilleau et al., 2021; Zenhausern et al., 2022) and listed in Table S1.

SsPp phase

Fig. 1b illustrates the ray path of the SsPp phase, where the Ss-leg of the ray path (the dashed line in red) is almost parallel to that of the direct SV phase (Ss). The major difference between the ray paths is the near- or post-critical Pp reflection at the base of Layer 1. Therefore, the travel-time difference between the direct Ss phase and SsPp phase can provide constraints on the average P-wave speed and thickness of Layer 1:

$$T_{SsPp-Ss} = 2H\eta_\beta = 2H\sqrt{\frac{1}{V_P^2} - p_\beta^2}, \quad (1)$$

Where η_β and p_β are the vertical and horizontal slowness (i.e., ray parameter) of the incident SV wave, respectively. V_P is the average P-wave speed in the layer, and H is its overall thickness.

We first calculated synthetic seismograms for the radial (R) and vertical (Z) components using a MATLAB package (Yu et al., 2017) based on the propagator method (Kennett, 2009) with a planar incident SV-wave. Using one of the models from the receiver function study (Knapmeyer-Endrun et al., 2021) with a Layer 1 thickness of 8 km and P-wave velocity of 3.0 km/s, we found that the simulated SsPp phase arrives about 4 s after the direct SV phase for marsquakes with an epicentral distance of 30 degrees (i.e., a ray parameter of 13.3 s/deg). This SsPp phase is observable on both the radial and vertical components (Fig. 1c).

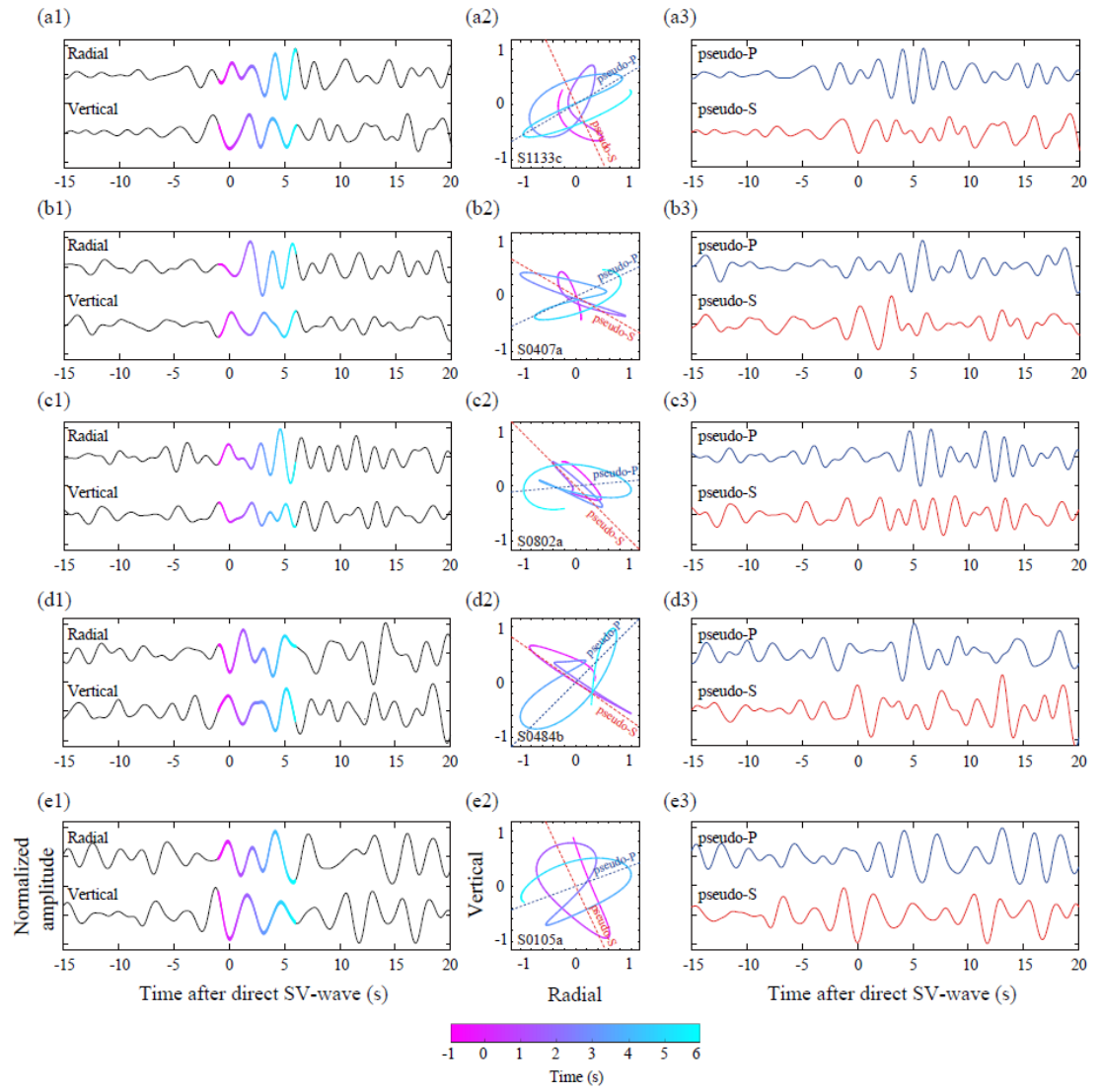
Particle motion analysis of the radial and vertical components of the synthetics shows that the first signal (at -1 to 2 s) and the second signal (at 3 to 5 s) have distinctive particle motions. Specifically, the first signal follows a linear trend in the second and fourth quadrants, and the second signal is polarized in the first and third quadrants (Fig. 1d). We can define pseudo-S and pseudo-P components according to the direction of these two sub-linear particle motions (Yu et al., 2013). On the pseudo-S component, the main phase is the direct SV phase at 0 s (Fig. 1e). On the pseudo-P component, there is no direct SV phase at 0 s, but a strong SsPp phase is visible at around 4 s (Fig. 1e).

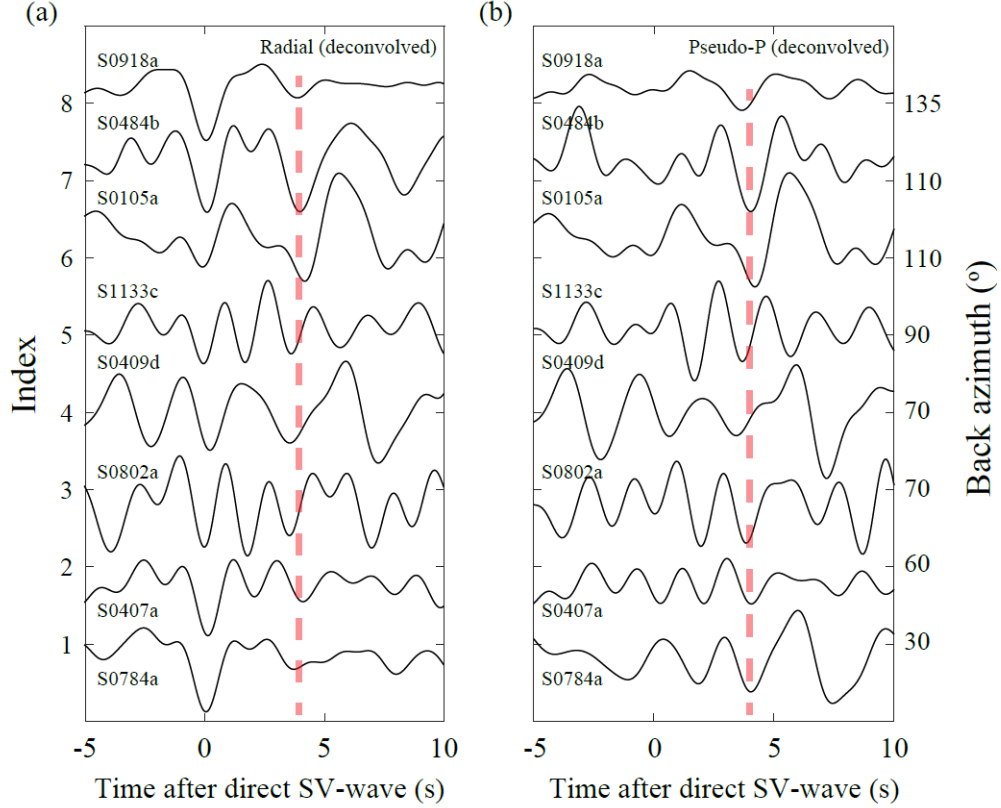
We applied the same particle motion analysis and the pseudo-P and S separation technique to the real data. Fig. 2 shows examples of quality-A event S1133c, quality-B events S0407a and S0802 (both back azimuths are around 65 degrees), and quality-B events S0484b and S0105a (with back azimuths of about 110 degrees). In Fig. 2, the start time (0 s) is selected based on the arrival time of the S-wave measured by MQS (Table S2), where the signal envelope is analyzed in multiple narrowband filters and the coherent start time in the largest possible bandwidth is selected (Clinton et al., 2021). In all cases, there are two linear trends in the particle motion analysis and there is a strong signal at around 4 to 5 s on the pseudo-P components.

Although the arrival times of the signals on the pseudo-P components are coherent, their waveforms vary between different events. This is mainly due to the different source time functions, which are indicated by the phase at 0 s on the pseudo-S components. To remove the effect of different kinds of source wavelets, we assumed the waveforms on the pseudo-S component to be an approximation of the source wavelet and deconvolved the pseudo-S component out of the pseudo-P component (Yu et al., 2013). Since we treated the source wavelet as a wave train (with a duration longer than 10 s, see Table S2), small discrepancies in the selection of the direct S-wave arrival (i.e., 0 s in Fig. 2) will not influence the results after the deconvolution.

After the deconvolution, all eight events show a consistent negative phase at around 3.5 - 4.3 s on the pseudo-P components (Fig. 3a, 3b, and Table S1), which is similar to the shape of the synthetic SsPp phase (Fig. 1e). This signal is more easily observable on the radial component after the deconvolution (Fig. 3a) than on the raw data (e.g., Fig. 2a).

We note that there are multiple peaks on both the radial and pseudo-P components for quality-A event S1133c after deconvolution, which are probably due to the complexity of the source time function (Fig. S2). Similar features have been observed for another four quality-A events (Fig. S3a). Regardless of these oscillations in these quality-A events, the negative pulse still falls into the same range (from 3.5 to 4.3 s) as seen for the quality-B events.





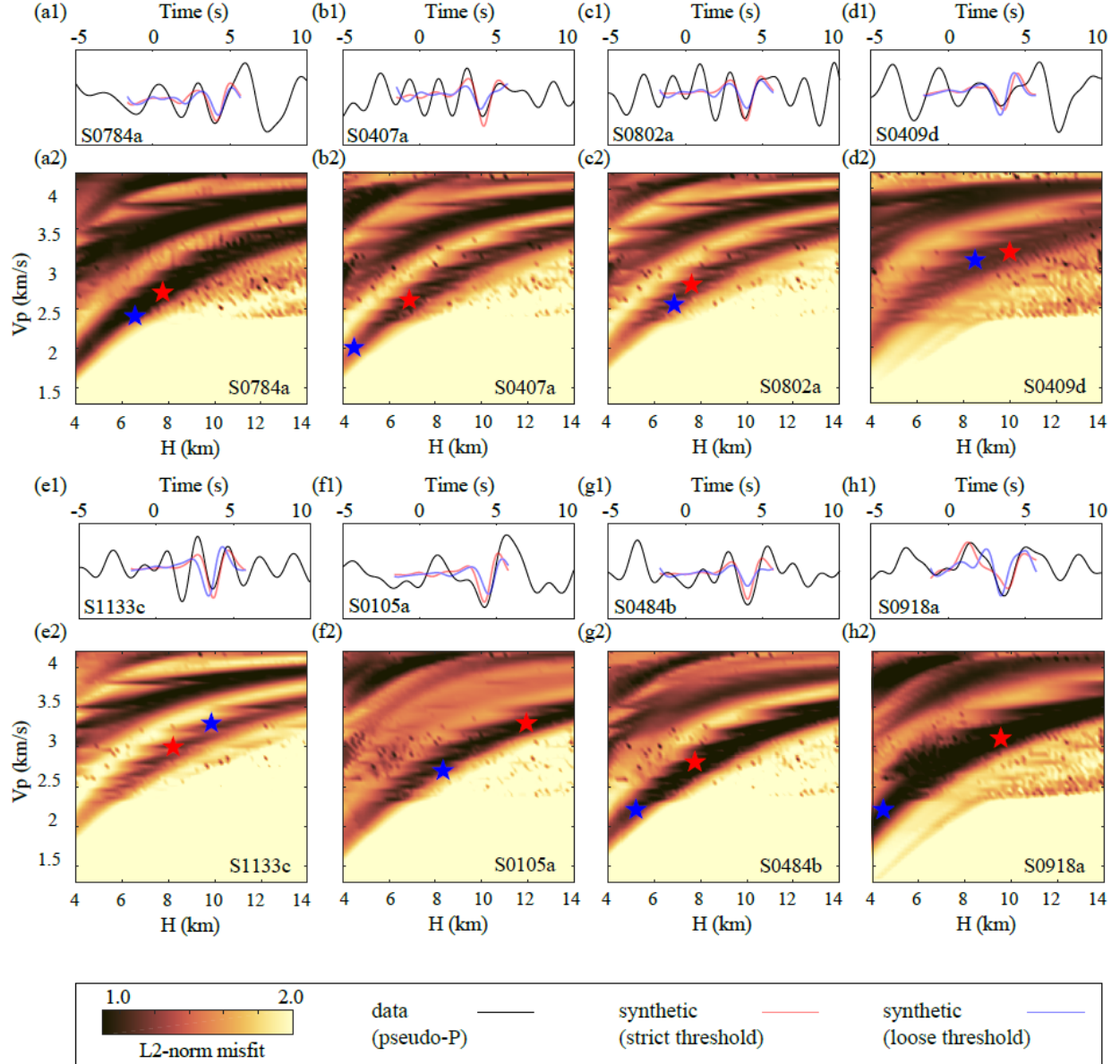
1.3 Constraints from SsPp

In the SsPp phase, there is a near- or post-critical Pp reflection at the base of Layer 1, and thus a phase shift might occur. When such a phase shift happens, it prevents us from accurately picking the arrival time of SsPp. Therefore, we prefer to perform a waveform comparison (between the data and the synthetics) rather than refer to equation (1), to constrain the model parameters (i.e., the average P-wave speed and thickness of Layer 1).

To compare the synthetic SsPp waveforms with the data, we applied the same processing (i.e., particle motion analysis, separation of the pseudo-P and pseudo-S components, deconvolution of the pseudo-S trace) to the synthetic waveforms. We found that the synthetic waveforms (i.e., the blue and red waveform in Fig. 4a1), generated by the acceptable models (i.e., corresponding to the blue and red stars in Fig. 4a2), match the pulse (3.5 – 4.3 s) in the data well (i.e., the black trace in Fig. 4a1) despite some complexities in the data (e.g., at 0 second for S0784a, and S0409d, and 6 seconds for S0784a, S0409d, and S0105a).

To quantify the waveform similarity between the data and the synthetics, we selected a time window from -1.0 to 5.3 s (indicated by the length of the red

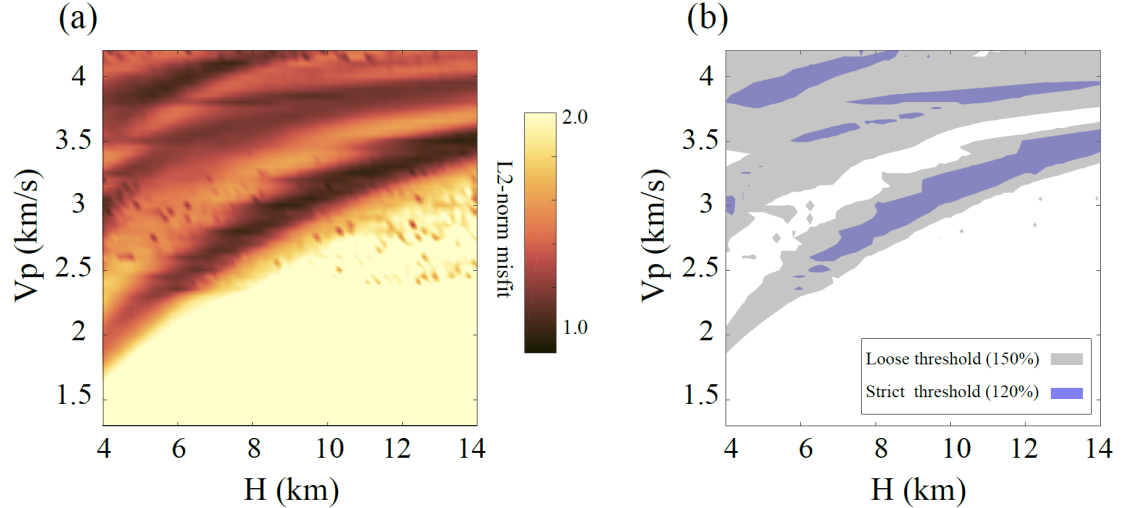
or blue synthetics in Fig. 4) to mainly focus on the SsPp phase. We chose the L2-norm of the waveform differences in the time domain as the misfit function to capture both the arrival time and amplitude information. We found that the average L2-norm misfit along the approximate diagonal (i.e., regions close to the predictions from the ray theory with equation (1)) is smaller than 1.0, confirming our identification of the SsPp phase.



Although these models predict waveforms that are similar to the data, trade-offs between model parameters (SV-wave speed and layer thickness) exist as shown in equation (1). To find all acceptable models, we performed forward modeling and sampled the P-wave speed (from 1.3 km/s to 4.2 km/s with an interval of 0.02 km/s) and layer thickness (from 4 km to 14 km with an interval of 0.05 km) of Layer 1. Since the velocity of the second layer will affect both the amplitude and the phase of the SsPp signal (Fig. S4), we also varied the velocity of the second layer (from 1.1 to 1.8 times the velocity of Layer 1 in 0.1 intervals). At each grid cell, we calculated synthetic waveforms, performed the particle motion analysis, separated the pseudo-P and pseudo-S components, deconvolved the assumed source wavelet (pseudo-S), and finally calculated the L2-norm misfit. The misfit maps are shown below the waveforms in Fig. 4. Models in the dark regions have smaller misfits and are thus more acceptable than models in the bright area. All the misfit maps similarly indicate a curved region on the diagonal consistent with equation (1).

To suppress the data noise, we averaged the L2-norm misfit maps (with different weights, see Supplementary Material, Section 1.1) to get the final constraints from SsPp (Fig. 5a). We first found the best-fitting model using the smallest misfit, then defined the range of acceptable models using a misfit threshold (i.e., strict and loose thresholds were set for misfits within 120% and 150% of the minimum misfit, respectively). Those strict and loose thresholds were set to extract the acceptable region of the model space (i.e., Fig 5b). We also see that there are two distinct sets of solutions that differ in the P-wave speeds (i.e., one along the approximate diagonal and the other near the upper left corner). In the results section, we will combine this analysis with results from the receiver function analyses to help us favor one over the other.

Although the choice of correlation threshold is arbitrary, we are confident our analysis is robust because we tested several thresholds and compared them with predictions from ray theory. For example, if we consider a smaller threshold value of 110% (of the minimum misfit), there are very few acceptable regions (in Fig. S5a). We also compared the acceptable regions (derived from the L2-norm misfit maps) with the ray-theory-based calculation using formula (1). The first-order trends are similar between these two approaches (Fig. S5). In addition, the choice of the misfit function (e.g., L2-norm, L1-norm, or cross-correlation coefficient) does not affect the pattern of the misfit map (Fig. S6).



We note, however, that there are discrepancies between our derived acceptable regions and the ray-theory-based predictions (Fig. S5). These arise because, when the velocity of the second layer is large enough, the SsPp is a post-critical reflection and a phase shift occurs. In such a case, the location of the negative pulse deviates from the actual arrival time of the SsPp phase (Fig. S4). Therefore we trust the results from the misfit map since the possible phase shift (for the critical P-p reflection off Layer 1) is included in the synthetics calculations. In addition, multiple sources of uncertainties are automatically included in the final misfit map such as the noise in the data, the duration of the pulse, and even finite-frequency effects.

Results

2.1 P-wave speed

Our study provides constraints on P-wave velocity in Layer 1 using the SsPp phase, which can be compared to the 20,000 acceptable 2-layer and 3-layer models of Knapmeyer-Endrun et al. (2021). In Fig. 6, we plotted the distribution of P-wave speed and thickness for Layer 1 using those 20,000 models in the 2-layer and 3-layer crust cases (Fig. 6a and c, respectively). In both cases, the models are located along a sub-linear trend reflecting the trade-offs between the wave speed and layer thickness.

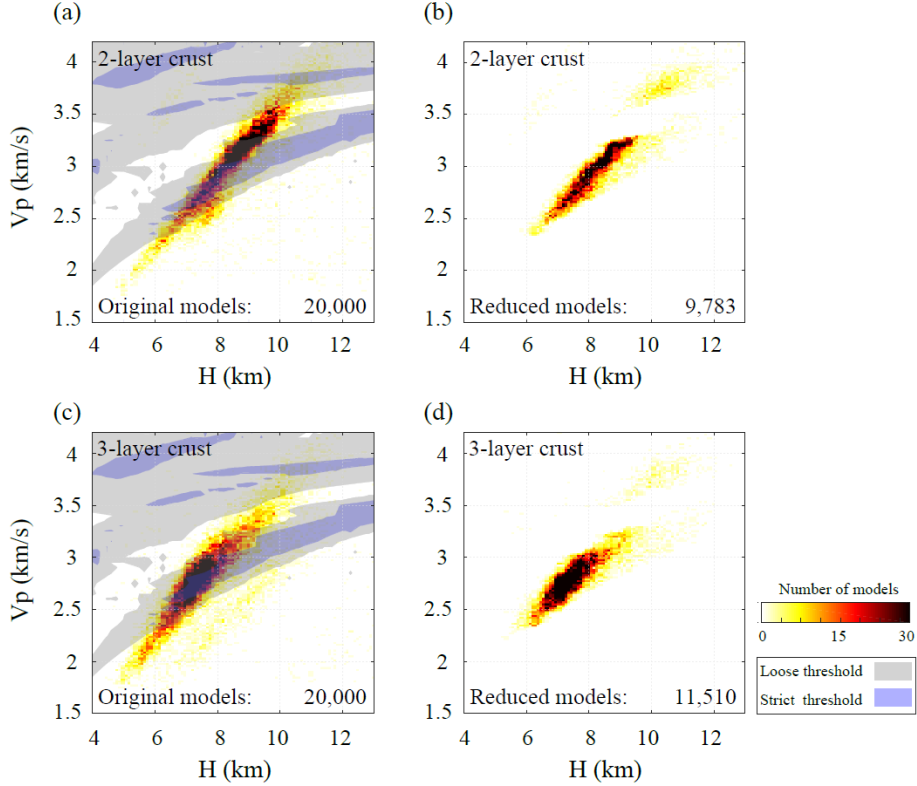
We superimposed the acceptable model space regions determined from our SsPp analysis for the strict and loose thresholds (blue and grey regions, respectively). For both the 2-layer (Fig. 6a) and 3-layer (Fig. 6c) case, acceptable regions derived from the SsPp analyses intersect with the models from Knapmeyer-Endrun et al. (2021). Because the acceptable ensemble of models derived from the SsPp analysis has a different slope than the models obtained with receiver

function, the trade-offs between model parameters and the number of possible models can be reduced. That is, models located at the intersection of the two regions are accepted by both the receiver function and the SsPp data. When they are outside the loose threshold contours, those models are rejected. Models lying in-between the two thresholds have a certain chance of being accepted:

$$P = \frac{L_{\text{loose}} - \text{misfit}}{L_{\text{loose}} - L_{\text{strict}}}, \quad (2)$$

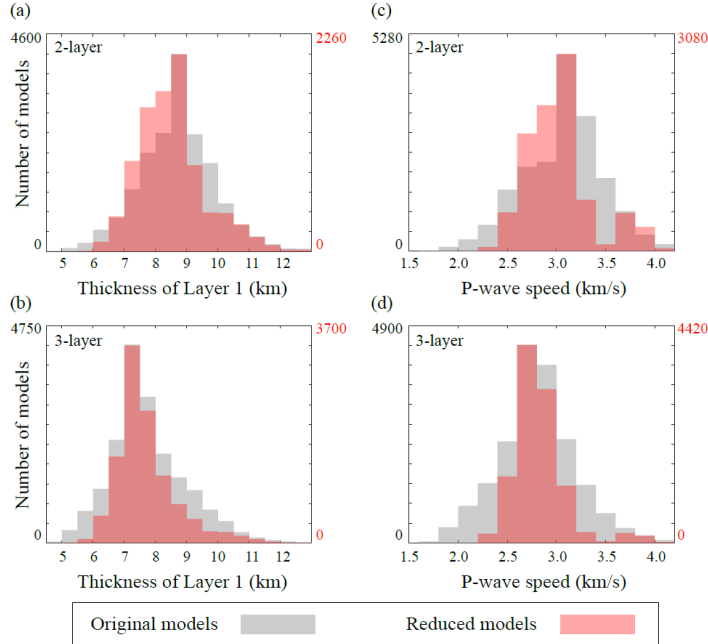
where P is the likelihood of being accepted, and L_{loose} and L_{strict} are the L2-norm of the loose (i.e., 150%) and strict threshold (i.e., 110%) we set in this study, respectively.

With this new constraint, the total number of possible models is reduced from 20,000 to 9,783 for the 2-layer crustal case, and from 20,000 to 11,510 for the 3-layer crustal case (Fig. 6b and 6d). The most prominent feature of these smaller model sets is a cut-off P-wave speed of about 3.3 km/s, showing that smaller wave speeds are preferred by the SsPp data. We also note that the solutions of the SsPp analysis with high wave speeds (near the upper left corner in Fig. 5) are inconsistent with the receiver function analysis.



2.2 P-wave speed and thickness of Layer 1

In Knapmeyer-Endrun et al. (2021), two ensembles of crustal models were shown to be compatible with the receiver function data: a 2-layer model and a 3-layer model. However, discrepancies were found between the two sets of models, for both the P-wave speed and the thickness of Layer 1 (i.e., grey histograms in Fig. 7): the preferred thickness for Layer 1 is 8.5-9.0 km for the 2-layer case and 7.0 - 7.5 km for the 3-layer case, and the preferred P-wave speed for Layer 1 is 3.0-3.5 km/s for the 2-layer case and 2.5-3.0 km/s for the 3-layer case. These discrepancies might be because the properties of Layer 1 (e.g., velocity and thickness) have to be able to explain both the Ps phase and its multiple PpPs phase for the 2-layer crustal case (Knapmeyer-Endrun et al., 2021).



The analyses we performed in the present work allow us to obtain new distributions of possible P-wave speed and thickness for Layer 1 (Cunningham and Lekic (2019); Liu et al. (2019)) in both the 2-layer case and the 3-layer case (i.e., red histograms in Fig. 7). Using the ensemble of models obtained with our additional constraints from the SsPp data, we found that the preferred thickness of Layer 1 for the 3-layer crust case remains unchanged (7.0 - 7.5 km). However, the preferred thickness for the 2-layer crust case is shallower (7.5 - 9.0 km) than in the original receiver function study (8.5 - 9.0 km, from Knapmeyer-Endrun et al. (2021)). The preferred P-wave speeds in both cases are centered between 2.5 - 3.2 km/s, which is also seen in Fig. 6. The reduced model set has thus slightly tighter constraints (less spread in the histogram) on the P-wave speed than on the layer thickness, which is a consequence of the small slope of the

acceptable regions in Fig. 6. In addition, the estimated P-wave speed and thickness of Layer 1 are more consistent between the two cases when adding our SsPp constraints to the original receiver function study. However, based solely on our SsPp analysis and the receiver function analysis of Knapmeyer-Endrun et al. (2021), we cannot distinguish between a 2-layer and 3-layer crust.

Discussion

3.1 Method Validation

The separation of the pseudo-SV and pseudo-P wave trains is key to removing the source-side scatterings and enhancing the signals from the structure. In this study, we estimated those based on a particle motion analysis (Yu et al., 2012). This approach is fully based on the data, and does not rely on a priori knowledge of the near-surface. However, the results could be affected by the presence of noise. To test the influence of the possible noise, we also applied a free-surface transform matrix (Kennett, 1991), constructed from prior information about the P- and S-wave speeds of the near-surface from Kim et al. (2021), to estimate the P- and SV-waveforms. Results show that the derived pseudo-S and pseudo-P wave trains from this free-surface transformation are consistent with those from the particle motion analysis (see Supplementary Material, Section 1.2).

To search for the acceptable models, we performed grid searches for three parameters: the average P-wave velocity and the thickness of Layer 1, and the P-wave velocity of the second layer. An alternative way to assess our results is to directly use the 40,000 receiver-function-derived models (Knapmeyer-Endrun et al. 2021) to calculate the synthetic SsPp waveforms and compare them with the SsPp data. Results show that both approaches exhibit the same first-order pattern: models with a P-wave velocity larger than 3.3 km/s are rejected. This implies that the upper limit of the P-wave velocity (at around 3.3 km/s) is required by the data and is not dependent on the inversion approach (see Supplementary Material, Section 1.3).

We further analyzed the model uncertainties resulting from location error (i.e., epicentral distance and back azimuth) and glitches (see Supplementary Material, Section 1.1). We also investigated the possible interferences with other signals (see Supplementary Material, Section 1.4), the sharpness and dip of the interface (see Supplementary Material, Section 1.5), the effects of different data types (i.e., displacement or velocity records, see Supplementary Material, Section 1.6), and compared our models with auto-correlation results (see Supplementary Material, Section 1.7). We concluded that our derived P-wave speed in Layer 1 (between 2.5 km/s and 3.3 km/s) is robust.

3.2 Origin of Layer 1

The low P-wave speed in Layer 1 indicates the presence of materials with low seismic velocity in the upper crust at the InSight landing site. Low seismic velocities, in turn, imply materials with low density (compared to the middle or lower crust), that could result from elevated porosity (e.g., Lognonné et al., 2020), low-density lithologies (including chemically altered lithologies), or a combination of intrinsically low-velocity materials and porosity (e.g., Wieczorek et al., 2022).

The near-surface geology and stratigraphy in the vicinity of the InSight landing site are now reasonably well understood although the constitution of the deeper crust (i.e., > 0.2 km) is less well constrained (Pan et al., 2017, 2020; Golombek et al., 2020; Warner et al., 2022). The subsurface at the InSight landing site includes a shallow impact-generated regolith (several meters thick) that grades into ~ 170 m of Early Amazonian to Hesperian basalt lava flows that are underlain by sedimentary rocks of the Noachian age (Golombek et al., 2017, 2018; Pan et al., 2020; Warner et al., 2022). Orbital imaging and spectral evidence from lithologies thought to be excavated in nearby craters suggest that rocks at greater depth are characterized by Fe/Mg-bearing phyllosilicates and are interpreted to be either Noachian sedimentary rocks (Warner et al., 2022; also see Pan et al., 2020) or aqueously altered Noachian igneous rocks (Pan et al., 2017), or presumably some combination, and that could extend to depths up to 5 km – possibly the entire thickness of Layer 1.

3.2.1 Porosity Effects

Since all of the possible Layer 1 lithologies (sedimentary, volcanic, altered Noachian basement) in the vicinity of the landing site could contain significant porosity, we first consider the influence of porosity alone on seismic wave speed.

Here, we assess how porosity affects the wave speed of typical Martian basaltic materials. This will provide us with a maximum allowable porosity, given that other materials (e.g., sedimentary rocks) have intrinsically lower wave speeds.

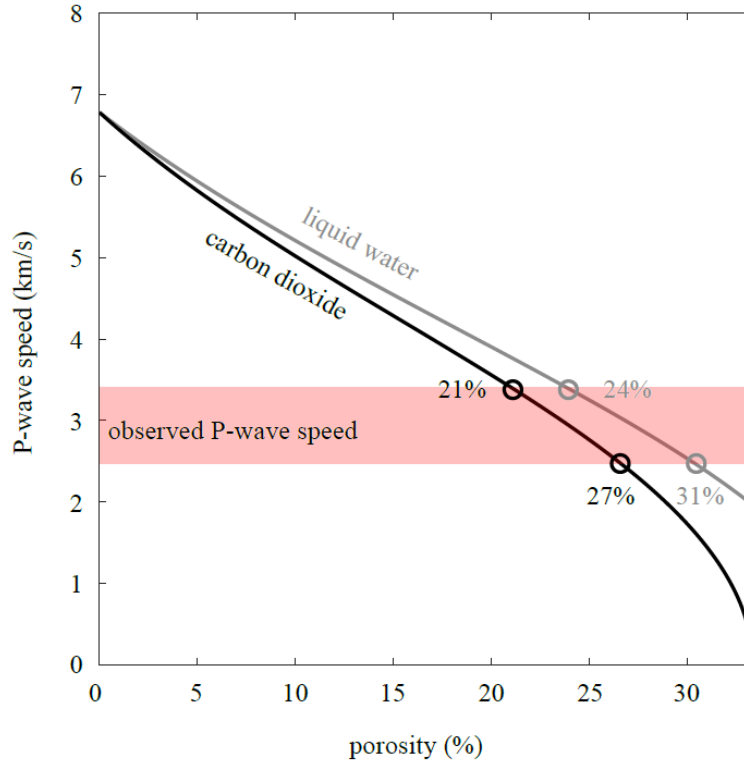
We make use of the scattering theory of Toksöz et al. (1976) to estimate the P-wave speeds of a given material as a function of porosity. As demonstrated in Heap (2019), the bulk seismic velocity depends upon the matrix composition, the amount of porosity, the composition of the material filling the pores, and the pore aspect ratio. We have performed similar calculations as in that study and compared the predicted wave speeds with our P-wave speed results for Layer 1 beneath the InSight lander. For the model setup, we assumed a basaltic composition for the matrix, given that basalts are the dominant rock type found near the surface of Mars (e.g., McSween et al., 2009). Such a composition could be representative of either basaltic lavas or the detrital grains of unaltered basaltic sediment (e.g., McLennan et al., 2019). After including a specified porosity, the pore space was filled with either atmospheric gas (e.g., carbon dioxide) or liquid

water. Manga and Wright (2021) demonstrated that the observed low S-wave speeds in the upper 8 km beneath the InSight lander preclude the existence of water ice in this layer (Knapmeyer-Endrun et al., 2021), so we did not consider this case further in our analysis.

We plotted our predicted P-wave speeds in Fig. 8. A seismic velocity of 6.8 km/s was assumed for non-porous basaltic materials (Christensen, 1972), a pore aspect ratio of 0.1 was assumed, and properties of the void filling materials were taken from Heap (2019). We see that as the porosity increases, the P-wave speed in the layer decreases, being reduced by a factor of two for porosities close to 20-25%. The P-wave velocity is somewhat larger when the pores are filled by liquid water than by atmospheric gas, but the difference is only moderate for the majority of the range of porosities that we consider. Our P-wave speeds for the upper 8 km of Mars from InSight data (from 2.5 to 3.3 km/s) can be accounted for by a porosity of 24-31% when the pores are filled by liquid water, or 21-27% when the pores are filled by atmospheric gas. If the pores were more spherical than our assumed aspect ratio of 0.1, the amount of required porosity would be greater (see Heap, 2019). In contrast, if the seismic velocity of the matrix materials was lower than assumed, the amount of required porosity would be reduced.

Our computed porosities are consistent with the range of values found for a variety of typical extrusive rocks at volcanoes on Earth, which can approach 30% (see data tabulated in Lesage et al., 2018) and for clastic sediments that often exceed 30% (e.g., Boggs, 2009). On the other hand, these porosities are somewhat higher than those directly measured in Martian meteorites, with porosities mostly in the range of 2-12% (Coulson et al., 2007).

Though near-surface volcanic deposits can form with high porosities over a range of length scales (from gas bubbles in magmas to evacuated lava tubes), impact cratering is an additional mechanism that can fracture and generate significant porosity in crustal materials. As an example, combined gravity and remote sensing data imply that the average porosity of the crust of the Moon is about 12% (Wieczorek et al. 2013) and that the porosity could be even higher for the uppermost crust (Besserrer et al. 2014). Analyses of feldspathic samples from the lunar highlands reveal impact-generated porosities that range from about 2 to 20% (Kiefer et al. 2012). Drill core samples from the central peak ring of the Chixulub impact basin have similar average porosities as the lunar samples, near 12% at depths near a kilometer, with values that reach as high as 20% at shallower depths (Rae et al., 2019). Drill cores from within the Reis impact crater on Earth also show the presence of up to about 30% porosity in the upper few hundred meters (Förstner 1967). Given the ancient age of the surface volcanic materials at the InSight landing site (from Hesperian to Early Amazonian, see Warner et al., 2022), combined with the presence of an ~10 m thick impact generated regolith at the surface in the vicinity of the landing site, impact processes could have plausibly contributed to high levels of porosity in the upper 8 km of the crust beneath the InSight lander.



3.2.2 Lithological Effects

When considering lithological effects, it is also convenient to think in terms of rock density since seismic velocities for several different possible lithologies are more difficult to directly predict in any systematic manner. Although it is well known that there is a relationship between seismic velocities and rock density, the detailed nature of that relationship is less certain (e.g., Brocher, 2005). Nevertheless, values of the P-wave speeds in the range of 2.5 to 3.3 km/s likely correspond to rock densities in the range of about 2000 to 2300 kg m⁻³ (Christensen and Salisbury, 1975; Gardner et al., 1974; Brocher, 2005) or, a reduction of about < 35-55% assuming an average crustal grain density of < 3100 kg m⁻³ (Wieczorek et al., 2022; also see Taylor and McLennan, 2009).

In Figure 8, we assumed that porosity-free upper crustal basaltic rocks have a P-wave speed of 6.8 km/s which is broadly consistent with the average crustal bulk density that is constrained to be < 3,100 kg m⁻³ (Wieczorek et al., 2022). However, recent findings from rover activities in Gale crater and lithologies preserved in the Martian meteorite breccia NWA7533 (and its numerous pairs) indicate that the early crust of Mars is lithologically diverse (e.g., Humayun et al., 2013; Cousin et al., 2017) with compositions ranging from picrobasalt (SiO₂ < 45%) through to alkali-rich intermediate-felsic compositions (SiO₂ >

60%). Wieczorek et al. (2022) estimated the grain densities for known igneous lithologies and found them to be in the range of 2,680 - 3,420 kg m⁻³, thus varying by over 25% relative. Accordingly, there is a possibility that at least some of the igneous materials making up the upper crust in the vicinity of InSight have porosity-free P-wave velocities that are lower than the 6.8 km/s assumed here.

The favored interpretation of the presence of several kilometers of Noachian sedimentary rocks beneath the landing site is consistent with our current understanding of the scale of the Martian sedimentary record. Based on geochemical mass balance, McLennan (2012) estimated the minimum size of the Martian sedimentary mass to be between 5e10²² and 5e10²³ g, which, assuming an average density of 2,000 kg m⁻³ (see below), corresponds to a global average thickness of 0.17-1.7 km. In several locations, sedimentary rock thicknesses are known to be very much greater. For example, the sedimentary sequence in Gale crater is measured to be 5 km (Grotzinger et al., 2015), the sedimentary sequence in Juventae Chasma (Valles Marineris) may be on the order of 3-6 km thick (Grotzinger and Milliken, 2012), and the Medusae Fossae Formation in places is up to 3 km thick (Bradley et al., 2002). Globally, the Martian sedimentary rock record is lithologically and mineralogically complex and influenced by a variety of sedimentary processes (e.g., chemical weathering, mineral sorting) and diagenetic processes (e.g., cementation, compaction, secondary porosity formation) (McLennan and Grotzinger, 2008; McLennan et al., 2019).

Although sedimentary rocks can contain large amounts of primary intergranular porosity, in many cases that porosity may be lost during compaction and/or filled by diagenetic cements during the lithification process (Boggs, 2009), and for Mars, such cements can be highly variable with respect to mineralogy (phyllosilicates, sulfates and chlorides of variable hydration state, amorphous silica and other amorphous, commonly hydrated, phases) (McLennan and Grotzinger, 2008; McLennan et al., 2019). Although such cements eliminate porosity, their densities can be significantly lower than the grain density of the clastic particles and so the overall effects on both bulk density and seismic velocities would be to lower them but it is not possible to make quantitative predictions.

There have been some attempts to independently constrain the densities of Martian sedimentary rocks. Using combined gravity and topography signatures, Ojha and Lewis (2018) estimated a bulk density of 1,765 ± 105 kg m⁻³ for the Medusae Fossae Formation (also see Watters et al., 2007), a notably low value that was attributed to the result from either high contents of water ice (Watters et al., 2007) or, more likely, elevated porosity (> 35% averaged over 1.5 km depth) (Ojha and Lewis, 2018). Using the Curiosity rover accelerometer to measure the gravity field (Lewis et al., 2019), and correcting for the gravity field resulting from the Gale impact, Johnson et al. (2021) estimated the mean bulk density of the sedimentary rocks in Gale crater to be 2,300 ± 130 kg m⁻³. This density was considered consistent with a porosity of 18 ± 6%, a value in turn consistent with lithified sedimentary rocks that have undergone about 4-5

km of burial compaction (Johnson et al., 2021).

Although considered less likely, another deep upper crustal lithology that may underlie the InSight landing site is aqueously altered Noachian igneous rocks, possibly similar to the rocks in the ancient highlands ~500 km to the southwest. Pan et al. (2017) examined the mineralogy of deeper crustal materials exposed in craters throughout the northern lowland and found a variable mixture of primary volcanic mafic minerals and a variety of hydrous minerals, dominated by Fe/Mg phyllosilicates, interpreted to have formed by aqueous alteration processes in the Noachian crust. The density of Fe/Mg phyllosilicates (e.g., nontronite, saponite) is mostly in the range of 2,200-2,300 kg m⁻³ (Anthony et al., 2002) and thus are also likely to lower the density of the primary crustal igneous materials.

3.3.3 Synthesis

From the above analysis, it is clear that porosity alone – in both sedimentary and volcanic rocks – could potentially explain the low P-wave speed observed in Layer 1. On the other hand, it is less likely that lithological factors alone, such as the presence of cemented sedimentary rocks, aqueously altered igneous rocks, or more felsic rocks, could do so. Nevertheless, our current understanding suggests that the upper crustal stratigraphy beneath the landing site is dominated by lithologies that have reduced densities related to the presence of secondary materials such as sedimentary cements and other hydrous alteration phases. Accordingly, our favored hypothesis is that a combination of low-density lithologies (cemented sedimentary rocks, intermediate-felsic igneous rocks, aqueously altered Noachian igneous rocks) almost certainly played a significant role in reducing P-wave speed. However, in addition to that, it is also necessary that significant primary porosity (and for sedimentary rocks, possibly secondary porosity) remained in many of these rocks.

A final issue is what is the origin of the seismic discontinuity at the base of Layer 1. Given the known thicknesses of sedimentary rocks on Mars, a Noachian sedimentary succession on the order of 7 km thickness is plausible and so one possibility is that the base of Layer 1 is essentially the base of a sedimentary rock sequence. If, on the other hand, aqueously altered igneous rocks dominate at these depths, then the boundary could also correspond to the maximum depth of aqueous alteration and therefore fluid flow.

In either case, it is likely that porosity also plays a significant role. Both compaction and viscous deformation will result in porosity reduction with depth. Gyalay et al. (2020) showed that the closure of pore space should occur over a narrow depth range of a few kilometers. Above this transition zone, the rocks retain their initial porosity, whereas below this transition zone all porosity is removed. The absolute depth of the transition zone depends upon the heat flow at the time when the porosity was created. If most porosities were created by impacts before 3.9 Ga, based on reasonable estimates of the surface heat flow at

that time, all porosity would have since been removed for depths greater than about 12-23 km (Wieczorek et al. 2022). Thus, if Layer 1 initially contained high porosities near 20-30% at 3.9 Ga, this porosity would remain to the present day. If Layer 1 instead formed at a later date (such as from sedimentary processes), these materials would also retain their initial porosity to the present day.

Accordingly, a combination of lithological change and pore reduction (or elimination) is a plausible mechanism to explain the seismic discontinuity at the base of Layer 1 and is also consistent with the known geological relationships in the vicinity of the InSight lander site.

Conclusions

We have analyzed one quality-A and seven quality-B broadband and low-frequency events and made the first coherent detection of the SsPp phase on Mars, which helps us constrain the crustal structure at the lander site. We found that quality-B marsquakes, with simpler source wavelets, behave better than the quality-A events when constraining the structure of the uppermost crustal layer (at about 8 km depth) when using the SsPp phase. We found coherent signals that are consistent with wave reflections off the first crustal interface, and this new phase confirms the existence of the ~ 8 km interface in the crust and the large wave speed (or impedance) contrast across it. The detected SsPp phase helped reduce the number of acceptable models used in the previous receiver function analysis of Knapmeyer-Endrun et al. (2021) from 20,000 models to about 10,000 models.

Using our new constraint from the SsPp phase, we determined that the P-wave speed in Layer 1 is between 2.5 km/s and 3.3 km/s, compared to the previous range of 2.0 - 3.5 km/s obtained by receiver function analysis. Based on these low P-wave speeds, the seismic properties of Layer 1 likely result primarily from the presence of relatively low density lithified sedimentary rocks and/or aqueously altered igneous rocks that also have a significant amount of porosity, possibly as much as $\sim 30\%$ by volume.

Open Research

Datasets (both the raw data and the deglitched data in SAC format, after removing the instrument response) for this research are available on the Zenodo repository: [10.5281/zenodo.6784826](https://zenodo.org/record/6784826).

Acknowledgments

J.L thank Tiezhao Bao and Weiliang Yin for sharing codes for the particle motion analysis, Ross Maguire for providing the Marsquakes downloading script,

and Brigitte Knapmeyer-Endrun for discussing the models from the receiver function study. The authors thank two anonymous reviewers and editor David Baratoux for their constructive comments. The misfit maps are plotted with the Scientific color maps (Crameri, F. 2018).

J.L. and C.B. were supported by NASA InSight PSP grant #80NSSC18K1679 and S.M.M. by NASA InSight PSP grant #80NSSC18K1622. P.L, E.S. and M.W. are supported by Agence Nationale de la Recherche (MAGIS, ANR-19-CE31-0008-08; IdEx Université Paris Cité, ANR-18-IDEX-0001) and by CNES for SEIS science support. M.S. thanks SANIMS (RTI2018-095594-B-I00).

This is InSight Contribution Number ICN 245. InSight seismic data presented here (http://dx.doi.org/10.18715/SEIS.INSIGHT.XB_2016) is publicly available through the Planetary Data System (PDS) Geosciences node, the Incorporated Research Institutions for Seismology (IRIS) Data Management Center under network code XB and through the Data center of Institut de Physique du Globe, Paris (<http://seis-insight.eu>). We acknowledge NASA, CNES, their partner agencies and Institutions (UKSA, SSO, DLR, JPL, IPGP-CNRS, ETHZ, IC, MPS-MPG) and the flight operations team at JPL, SISMOC, MSDS, IRIS-DMC and PDS for providing SEED SEIS data.

References

1. Anthony, J. W., Bideaux, R. A., Bladh, K. W., Nichols, M. C. (Eds.), 2002. Handbook of Mineralogy, Mineralogical Society of America (Chantilly, VA, 20151-1110, USA) <http://www.handbookofmineralogy.org/>
2. Banerdt, W.B., Smrekar, S.E., Banfield, D., Giardini, D., Golombek, M., Johnson, C.L., Lognonné, P., Spiga, A., Spohn, T., Perrin, C. and Stähler, S.C., 2020. Initial results from the InSight mission on Mars. *Nature Geoscience*, 13(3), pp.183-189.
3. Boggs Jr., S., 2009. Petrology of Sedimentary Rocks, 2nd Ed. Cambridge University Press, 600pp.
4. Bradley, B. A., Sakimoto, S. E., Frey, H., Zimbelman, J. R., 2002. Medusae Fossae Formation: New perspectives from Mars Global Surveyor. *Journal of Geophysical Research – Planets*, 107, E85050, doi:10.1029/2001JE001537.
5. Brocher, T.M., 2005. Empirical relations between elastic wavespeeds and density in the Earth's crust. *Bulletin of the seismological Society of America*, 95(6), pp.2081-2092.
6. Brown, G.C. and Mussett, A.E., 1993. The Inaccessible Earth: An Integrated View of its Structure and Composition, 276 pp.
7. Chen, Qing, and Wang-Ping Chen. "Toward Simultaneous Determination of Bulk Crustal Properties Using Virtual Deep Seismic Sounding Toward Si-

- multaneous Determination of Bulk Crustal Properties Using Virtual Deep Seismic Sounding.” *Bulletin of the Seismological Society of America* 110.3 (2020): 1387-1392.
8. Chen, W.P., Yu, C.Q., Tseng, T.L., Yang, Z., Wang, C.Y., Ning, J. and Leonard, T., 2013. Moho, seismogenesis, and rheology of the lithosphere. *Tectonophysics*, 609, pp.491-503.
 9. Chen, W.P. and Jiang, Y., 2020. Undulating Moho beneath a near-uniform surface of central Tibet. *Earth and Planetary Science Letters*, 543, p.116343.
 10. Christensen, N. I., Salisbury, M. W., 1975. Structure and constitution of the lower oceanic crust. *Reviews of Geophysics and Space Physics*, 13, 57-86.
 11. Christensen, N. I. (1972). Compressional and shear wave velocities at pressures to 10 kilobars for basalts from the East Pacific Rise. *Geophysical Journal International*, 28(5), 425-429.
 12. Clinton, J. F., Ceylan, S., van Driel, M., Giardini, D., Stähler, S. C., Böse, M., Charalambous, C., Dahmen, N. L., Horleston, A., Kawamura, T., et al., 2021. The marsquake catalogue from InSight, sols 0–478, *Physics of the Earth and Planetary Interiors*, 310, 106595.
 13. Compaire, N., Margerin, L., Garcia, R. F., Pinot, B., Calvet, M., Orhand-Mainsant, G., Kim, D., Lekic, V., Tauzin, B., Schimmel, M., et al., 2021. Autocorrelation of the ground vibrations recorded by the seis-insight seismometer on mars, *Journal of Geophysical Research: Planets*, 126(4), e2020JE006498.
 14. Coulson, I. M., Beech, M., Nie, W., 2007. Physical properties of Martian meteorites: Porosity and density measurements. *Meteoritics and Planetary Science*, 42, 2043-2054.
 15. Cousin, A., Sautter, V., Payré, V., Forni, O., Mangold, N. et al., 2017. Classification of igneous rocks analyzed by ChemCam at Gale crater. *Icarus*, 288, 265-283.
 16. Consolmagno, G. J., Britt, D. T., & Macke, R. J. (2008). The significance of meteorite density and porosity. *Geochemistry*, 68(1), 1-29.
 17. Crameri, F. (2018). Scientific colour maps. Zenodo. <http://doi.org/10.5281/zenodo.1243862>
 18. Cunningham, E. and Lekic, V., 2019. Constraining crustal structure in the presence of sediment: a multiple converted wave approach. *Geophysical Journal International*, 219(1), pp.313-327.
 19. Deng, S., & Levander, A. (2020). Autocorrelation reflectivity of mars. *Geophysical Research Letters*, 47, e2020GL089630.

20. Drilleau, M., Samuel, H., Garcia, R., Rivoldini, A., Perrin, C., Michaut, C., Wiczorek, M., Tauzin B., Lognonne, P., and Banerdt, B. W. (2021). Marsquake locations and 1-D seismic models for Mars from InSight data". In Revision.
21. Durán, C., A. Khan, S. Ceylan, G. Zenhäusern, S. Stähler, J. F. Clinton, and D. Giardini. "Seismology on Mars: An analysis of direct, reflected, and converted seismic body waves with implications for interior structure." *Physics of the Earth and Planetary Interiors* 325 (2022): 106851.
22. Förstner, U. (1967). Petrographische Untersuchungen des Suevit aus den Bohrungen Deiningen und Wörnitzostheim im Ries von Nördlingen. *Contr. Mineral. and Petrol.* 15, 281–308.
23. Gardner, G. H. F., Gardner, L. W., Gregory, A. R., 1974. Formation velocity and density – the diagnostic basics for stratigraphic traps. *Geophysics*, 39, 770-780.
24. Golombek, M., Grott, M., Kargl, G., Andrade, J., Marshall, J., Warner, N., et al. (2018). Geology and physical properties investigations by the InSight Lander. *Space Science Review*, 214, 84. <https://doi.org/10.1007/s11214-018-0512-7>
25. Golombek, M., Kass, D., Williams, N., Warner, N., Daubar, I., Piqueux, S., et al. (2020). Assessment of InSight landing site predictions. *Journal of Geophysical Research: Planets*, 125. <https://doi.org/10.1029/2020JE006502>
26. Golombek, M., Kipp, D., Warner, N., Daubar, I. J., Ferguson, R., Kirk, R. L., et al. (2017). Selection of the InSight landing site. *Space Science Review*, 211, 5–95. <https://doi.org/10.1007/s11214-016-0321-9>
27. Golombek, M., Warner, N. H., Grant, J. A., Hauber, E., Ansan, V. et al., 2020. Geology of the InSight landing site on Mars. *Nature Communications*, 11, 1014.
28. Grotzinger, J. P., Gupta, S., Malin, M. C., Rubin, D. M., Schieber, J. et al. (2015) Deposition, exhumation, and paleoclimate of an ancient lake deposit, Gale Crater, Mars. *Science*, 350, aac7575, doi:10.1126/science.aac7575.
29. Grotzinger, J. P., Milliken, R. E., 2012. The sedimentary rock record of Mars: Distribution, origins, and global stratigraphy. In: J. P. Grotzinger and R. E. Milliken (eds.) *Mars Sedimentology*, SEPM Spec. Publ. 102, 1-48.
30. Gyalay, S., Nimmo, F., Plesa, A.-C., Wiczorek, M., 2020. Constraints on thermal history of Mars from depth of pore closure below InSight. *Geophysical Research Letters*, 47, e2020G1088653.

31. Heap, M. J. (2019). P-and S-wave velocity of dry, water-saturated, and frozen basalt: Implications for the interpretation of Martian seismic data. *Icarus*, 330, 11-15.
32. Humayun, M., Nemchin, A., Zanda, B., Hewins, R. H., Grange, M. et al., 2013. Origin and age of the earliest Martian crust from meteorite NWA 7533. *Nature*, 503, 513-516.
33. InSight Marsquake Service, 2020. Mars Seismic Catalogue, InSight Mission; V1 2020-01-02.
34. InSight Marsquake Service, 2021. Mars Seismic Catalogue, InSight Mission; V7 2021-08-25.
35. InSight Marsquake Service, 2021. Mars Seismic Catalogue, InSight Mission; V8 2021-10-06.
36. InSight Marsquake Service, 2022. Mars Seismic Catalogue, InSight Mission; V9 upcoming.
37. InSight Marsquake Service, 2022. Mars Seismic Catalogue, InSight Mission; V10 upcoming.
38. InSight Mars SEIS Data Service. 2019. SEIS raw data, Insight Mission. IPGP, JPL, CNES, ETHZ, ICL, MPS, ISAE-Supaero, LPG, MFSC.
39. InSight SEIS Data Bundle. 2021. PDS Geosciences (GEO) Node.
40. InSight Mars SEIS Data Service. (2019). SEIS raw data, Insight Mission. IPGP, JPL, CNES, ETHZ, ICL, MPS, ISAE-Supaero, LPG, MFSC. https://doi.org/10.18715/SEIS.INSIGHT.XB_2016
41. Johnson, B. C., Milliken, R. E., Lewis, K. W., Collins, G. S., 2021. Impact generated porosity in Gale crater and implications for the density of sedimentary rocks in lower Aeolis Mons. *Icarus*, 366, 114539.
42. Kang, D., Yu, C., Ning, J. and Chen, W.P., 2016. Simultaneous determination of crustal thickness and P wavespeed by virtual deep seismic sounding (VDSS). *Seismological Research Letters*, 87(5), pp.1104-1111.
43. Kennett, B. L. N. (1991). The removal of free surface interactions from three-component seismograms. *Geophysical Journal International*, 104(1), 153– 154.
44. Kennett, B. L. N., & Engdahl, E. R. (1991). Traveltimes for global earthquake location and phase identification. *Geophysical Journal International*, 105(2), 429-465.
45. Kennett, B.L.N., 2009. *Seismic wave propagation in stratified media*, ANU Press.
46. Khan, A., Ceylan, S., van Driel, M., Giardini, D., Lognonné, P., Samuel, H., Schmerr, N.C., Stähler, S.C., Duran, A.C., Huang, Q. and Kim, D.,

2021. Upper mantle structure of Mars from InSight seismic data. *Science*, 373(6553), pp.434-438.
47. Kiefer, Walter S., Robert J. Macke, Daniel T. Britt, Anthony J. Irving, and Guy J. Consolmagno. "The density and porosity of lunar rocks." *Geophysical Research Letters* 39, no. 7 (2012).
 48. Kim, D., Lekić, V., Irving, J.C.E., Schmerr, N., Knapmeyer-Endrun, B., Joshi, R., Panning, M.P., Tauzin, B., Karakostas, F., Maguire, R. and Huang, Q., (2021a). Improving constraints on planetary interiors with PPS receiver functions. *Journal of Geophysical Research: Planets*, 126(11), p.e2021JE006983.
 49. Kim, D., Davis, P., Lekić, V., Maguire, R., Compaire, N., Schimmel, M., ... & Banerdt, W. B. (2021b). Potential pitfalls in the analysis and structural interpretation of seismic data from the Mars InSight mission. *Bulletin of the Seismological Society of America*, 111(6), 2982-3002.
 50. Knapmeyer-Endrun, B., Panning, M. P., Bissig, F., Joshi, R., Khan, A., Kim, D., Lekic, V., Tauzin, B., Tharimena, S., Plasman, M., et al., 2021. Thickness and structure of the martian crust from InSight seismic data, *Science*, 373(6553), 438–443.
 51. Laske, Gabi, Guy Masters, Zhitu Ma, and Mike Pasyanos. "Update on CRUST1. 0—A 1-degree global model of Earth's crust." In *Geophys. res. abstr.*, vol. 15, p. 2658. 2013.
 52. Lesage, P., Heap, M. J., & Kushnir, A. (2018). A generic model for the shallow velocity structure of volcanoes. *Journal of Volcanology and Geothermal Research*, 356, 114-126.
 53. Lewis, K. W., Peters, S., Gonter, K., Morrison, S., Schmerr, N., Vasavade, A. R., Gabriel, T., 2019. A surface gravity traverse on Mars indicates low bedrock density at Gale crater. *Science*, 363, 535-537.
 54. Li, J., Beghein, C., Wookey, J., Davis, P., Lognonné, P., Schimmel, M., Stutzmann, E., Golombek, M., Montagner, J.P. and Banerdt, W.B., 2022. Evidence for crustal seismic anisotropy at the InSight lander site. *Earth and Planetary Science Letters*, 593, p.117654.
 55. Liu, Tianze, Simon L. Klemperer, Gabriel Ferragut, and Chunquan Yu. "Post-critical SsPmp and its applications to Virtual Deep Seismic Sounding (VDSS)-2: 1-D imaging of the crust/mantle and joint constraints with receiver functions." *Geophysical Journal International* 219, no. 2 (2019): 1334-1347.
 56. Lognonné, P., Banerdt, W.B., Giardini, D., Pike, W.T., Christensen, U., Laudet, P., De Raucourt, S., Zweifel, P., Calcutt, S., Bierwirth, M. and Hurst, K.J., 2019. SEIS: Insight's seismic experiment for internal structure of Mars. *Space Science Reviews*, 215(1).

57. Lognonné, P., Banerdt, W., Pike, W., Giardini, D., Christensen, U., Garcia, R. F., Kawamura, T., Kedar, S., Knapmeyer-Endrun, B., Margerin, L., et al., 2020. Constraints on the shallow elastic and anelastic structure of Mars from InSight seismic data, *Nature Geoscience*, 13(3), 213–220.
58. Lognonné, P., Banerdt, W.B., Pike, W.T., Giardini, D., Christensen, U., Garcia, R.F., Kawamura, T., Kedar, S., Knapmeyer-Endrun, B., Margerin, L. and Nimmo, F., 2020. Constraints on the shallow elastic and anelastic structure of Mars from InSight seismic data. *Nature Geoscience*, 13(3), pp.213-220.
59. Manga, M., & Wright, V. (2021). No cryosphere-confined aquifer below InSight on Mars. *Geophysical Research Letters*, 48(8), e2021GL093127.
60. McLennan, S. M., 2012. Geochemistry of sedimentary processes on Mars. In: J. P. Grotzinger and R. E. Milliken (eds.) *Mars Sedimentology*, SEPM Spec. Publ. 102, 119-138.
61. McLennan, S. M., Grotzinger, J. P., 2008. The sedimentary rock cycle of Mars. In: J. F. Bell III (ed.) *The Martian Surface: Composition, Mineralogy, and Physical Properties*. Cambridge Univ. Press (Cambridge), pp. 541-577.
62. McLennan, S. M., Grotzinger, J. P., Hurowitz, J. A., Tosca, N. J., 2019. The sedimentary cycle on early Mars. *Annual Review of Earth and Planetary Science*, 166, 110-130.
63. McSween Jr, H. Y., Taylor, G. J., & Wyatt, M. B. (2009). Elemental composition of the Martian crust. *science*, 324(5928), 736-739.
64. Milbury, C., B. C. Johnson, H. J. Melosh, G. S. Collins, D. M. Blair, J. M. Soderblom, F. Nimmo, C. J. Bierson, R. J. Phillips, and M. T. Zuber. "Preimpact porosity controls the gravity signature of lunar craters." *Geophysical Research Letters* 42, no. 22 (2015): 9711-9716.
65. Ojha, L., Lewis, K., 2018. The density of the Medusae Fossae Formation: Implications for its composition, origin, and importance in Martian History. *Journal of Geophysical Research – Planets*, 123, 1368-1379.
66. Owens, T.J. and Zandt, G., 1997. Implications of crustal property variations for models of Tibetan plateau evolution. *Nature*, 387(6628), pp.37-43.
67. Pan, L., Ehlmann, B. L., Carter, J., Ernst, C. M., 2017. The stratigraphy and history of Mars' northern lowlands through mineralogy of impact craters: A comprehensive survey. *Journal of Geophysical Research – Planets*, 122, 1824-1854.
68. Pan, L., Quantin-Nataf, C., Tauzin, B., Michaut, C., Golombek, M. et al., 2020. Crust stratigraphy and heterogeneities of the first kilometers at

the dichotomy boundary in western Elysium Planitia and implications for InSight lander. *Icarus*, 338, 113511

69. Rae, A. S., Collins, G. S., Morgan, J. V., Salge, T., Christeson, G. L., Leung, J., ... & IODP-ICDP Expedition 364 Scientists. (2019). Impact-induced porosity and microfracturing at the Chicxulub impact structure. *Journal of Geophysical Research: Planets*, 124(7), 1960-1978.
70. Schimmel, M., Stutzmann, E., Lognonné, P., Compaire, N., Davis, P., Drilleau, M., Garcia, R., Kim, D., Knapmeyer-Endrun, B., Lekic, V., et al., 2021. Seismic noise autocorrelations on Mars, Earth and Space Science, p. e2021EA001755.
71. Scholz, J.-R., Widmer-Schmidrig, R., Davis, P., Lognonné, P., Pinot, B., Garcia, R. F., Hurst, K., Pou, L., Nimmo, F., Barkaoui, S., et al., 2020. Detection, analysis, and removal of glitches from InSight's seismic data from Mars, Earth and Space Science, 7(11), e2020EA001317.
72. Smith, D.E., Zuber, M.T., Frey, H.V., Garvin, J.B., Head, J.W., Muhleman, D.O., Pettengill, G.H., Phillips, R.J., Solomon, S.C., Zwally, H.J. and Banerdt, W.B., 2001. Mars Orbiter Laser Altimeter: Experiment summary after the first year of global mapping of Mars. *Journal of Geophysical Research: Planets*, 106(E10), pp.23689-23722.
73. Soderblom, Jason M., Alexander J. Evans, Brandon C. Johnson, H. Jay Melosh, Katarina Miljković, Roger J. Phillips, Jeffrey C. Andrews-Hanna et al. "The fractured Moon: Production and saturation of porosity in the lunar highlands from impact cratering." *Geophysical Research Letters* 42, no. 17 (2015): 6939-6944.
74. Stähler, S. C., Khan, A., Banerdt, W. B., Lognonné, P., Giardini, D., Ceylan, S., Drilleau, M., Duran, A. C., Garcia, R. F., Huang, Q., et al., 2021. Seismic detection of the martian core, *Science*, 373(6553), 443-448.
75. Taylor, S. R., McLennan, S. M., 2009. *Planetary Crusts: Their Composition, Origin and Evolution*. Cambridge University Press, 378pp.
76. Tseng, T.L., Chen, W.P. and Nowack, R.L., 2009. Northward thinning of Tibetan crust revealed by virtual seismic profiles: *Geophysics Research Letters*.
77. Wang, R., 1999. A simple orthonormalization method for stable and efficient computation of Green's functions, *Bulletin of the Seismological Society of America*, 89(3), 733-741.
78. Warner, N. H., Golombek, M. P., Ansan, V., Marteau, E., Williams, N. et al., 2022. In situ and orbital stratigraphic characterization of the InSight landing site – A type example of a regolith-covered lava plain on Mars. *Journal of Geophysical Research – Planets*, 127, e2022JE007232.

79. Watters, T. R., Campbell, B., Carter, L., Leuschen, C. J., Plaut, J. J. et al., 2007. Radar sounding of the Medusae Fossae Formation Mars: Equatorial ice or dry, low density deposits? *Science*, 318, 1125-1128.
80. Wieczorek, Mark A., Gregory A. Neumann, Francis Nimmo, Walter S. Kiefer, G. Jeffrey Taylor, H. Jay Melosh, Roger J. Phillips et al. "The crust of the Moon as seen by GRAIL." *Science* 339, no. 6120 (2013): 671-675.
81. Wieczorek, M.A., Broquet, A., McLennan, S.M., Rivoldini, A., Golombek, M., Antonangeli, D., Beghein, C., Giardini, D., Gudkova, T., Gyalay, S. and Johnson, C.L., 2022. InSight constraints on the global character of the Martian crust. *Journal of Geophysical Research: Planets*, p.e2022JE007298.
82. Yu, C.Q., Chen, W.P., Ning, J.Y., Tao, K., Tseng, T.L., Fang, X.D., Chen, Y.J. and van der Hilst, R.D., 2012. Thick crust beneath the Ordos plateau: Implications for instability of the North China craton. *Earth and Planetary Science Letters*, 357, pp.366-375.
83. Yu, C.Q., Chen, W.P. and van der Hilst, R.D., 2013. Removing source-side scattering for virtual deep seismic sounding (VDSS). *Geophysical Journal International*, 195(3), pp.1932-1941.
84. Yu, C., Chen, W.P. and van der Hilst, R.D., 2016. Constraints on residual topography and crustal properties in the western United States from virtual deep seismic sounding. *Journal of Geophysical Research: Solid Earth*, 121(8), pp.5917-5930.
85. Yu, C., Zheng, Y. and Shang, X., 2017. Crazyseismic: A MATLAB GUI-based software package for passive seismic data preprocessing. *Seismological Research Letters*, 88(2A), pp.410-415.
86. Zandt, G. and Randall, G.E., 1985. Observations of shear-coupled P waves. *Geophysical Research Letters*, 12(9), pp.565-568.
87. Zenhäusern, G., Stähler, S.C., Clinton, J.F., Giardini, D., Ceylan, S. and Garcia, R.F., 2022. Low-Frequency Marsquakes and Where to Find Them: Back Azimuth Determination Using a Polarization Analysis Approach. *Bulletin of the Seismological Society of America*.
88. Zhou, L., Chen, W.P. and Ozalaybey, S., 2000. Seismic properties of the central Indian shield. *Bulletin of the Seismological Society of America*, 90(5), pp.1295-1304.